Cell

Resource

Spatial proteomics in neurons at single-protein resolution

Graphical abstract

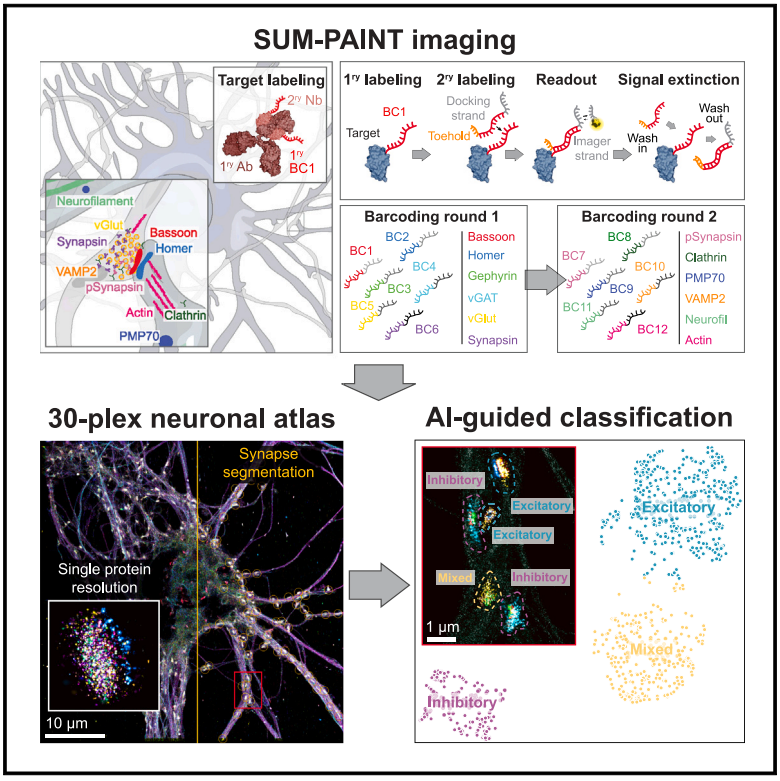

Highlights

- Development of SUM-PAINT enables high-throughput DNA-PAINT multiplexing
- 30-plex, 3D neuron atlas at single-protein resolution
- AI-guided analysis enables evaluation of high-dimensional SUM-PAINT datasets
- Discovery of a new synapse subtype characterized by VGlut1^{+} and Gephyrin^{+}

Authors

Eduard M. Unterauer, Sayedali Shetab Boushehri, Kristina Jevdokimenko, ..., Felipe Opazo, Eugenio F. Fornasiero, Ralf Jungmann

Correspondence

efornas@gwdg.de (E.F.F.), jungmann@biochem.mpg.de (R.J.)

In brief

Development of SUM-PAINT, an approach that is capable of potentially unlimited super-resolution multiplexing, enables rapid visualization of distinct synapse types at single-molecule resolution.

Unterauer et al., 2024, Cell *187*, 1785–1800
March 28, 2024
https://doi.org/10.1016/j.cell.2024.02.045

CellPress

Cell

CellPress
OPEN ACCESS

Resource

Spatial proteomics in neurons at single-protein resolution

Eduard M. Unterauer,[1,2,11] Sayedali Shetab Boushehri,[3,4,5,11] Kristina Jevdokimenko,[6,11] Luciano A. Masullo,[1] Mahipal Ganji,[1,7] Shama Sograte-Idrissi,[6,8] Rafal Kowalewski,[1,2] Sebastian Strauss,[1,2] Susanne C.M. Reinhardt,[1,2] Ana Perovic,[1] Carsten Marr,[3,5] Felipe Opazo,[6,8,9] Eugenio F. Fornasiero,[6,10,*] and Ralf Jungmann[1,2,12,*]

[1]Max Planck Institute of Biochemistry, Planegg, Germany
[2]Faculty of Physics and Center for NanoScience, Ludwig-Maximilians-Universität, Munich, Germany
[3]Institute of AI for Health, Helmholtz Zentrum München - German Research Center for Environmental Health, Neuherberg, Germany
[4]Data & Analytics, Roche Pharma Research and Early Development, Roche Innovation Center Munich, Munich, Germany
[5]Department of Mathematics, Technical University of Munich, Munich, Germany
[6]Institute of Neuro- and Sensory Physiology, University Medical Center Göttingen, Göttingen, Germany
[7]Department of Biochemistry, Indian Institute of Science, Bangalore, India
[8]Center for Biostructural Imaging of Neurodegeneration, University Medical Center Göttingen, Göttingen, Germany
[9]NanoTag Biotechnologies GmbH, Göttingen, Germany
[10]Department of Life Sciences, University of Trieste, Trieste, Italy
[11]These authors contributed equally
[12]Lead contact
*Correspondence: efornas@gwdg.de (E.F.F.), jungmann@biochem.mpg.de (R.J.)
https://doi.org/10.1016/j.cell.2024.02.045

SUMMARY

To understand biological processes, it is necessary to reveal the molecular heterogeneity of cells by gaining access to the location and interaction of all biomolecules. Significant advances were achieved by super-resolution microscopy, but such methods are still far from reaching the multiplexing capacity of proteomics. Here, we introduce secondary label-based unlimited multiplexed DNA-PAINT (SUM-PAINT), a high-throughput imaging method that is capable of achieving virtually unlimited multiplexing at better than 15 nm resolution. Using SUM-PAINT, we generated 30-plex single-molecule resolved datasets in neurons and adapted omics-inspired analysis for data exploration. This allowed us to reveal the complexity of synaptic heterogeneity, leading to the discovery of a distinct synapse type. We not only provide a resource for researchers, but also an integrated acquisition and analysis workflow for comprehensive spatial proteomics at single-protein resolution.

INTRODUCTION

One of the key goals of life science research is to understand living systems from the level of whole organisms, through the assembly of complex cellular networks, to the organization and interaction of individual biomolecules. To achieve this, we need technologies that can quantitatively measure all biomolecules and their spatial interactions. Omics techniques are poised to provide this capability. Among these, sequencing or mass spectrometry have had a profound impact by quantifying nucleic acid and protein abundance. However, to fully understand biological processes and functions, it is necessary to quantify the molecular heterogeneity of cells and subcellular assemblies by revealing the location and interaction of all biomolecules. This goal has been the focus of spatial omics techniques, which provide both absolute quantification and subcellular localization.

Methods such as MERFISH[1] and seqFISH+[2] provide spatially resolved transcriptomics and genomics, recently contributing to the assembly of cell atlases depicting age-related changes in mouse frontal cortices,[3] as well as characterizing the chromatin states and nuclear organization within specific cell types.[4] However, while these approaches to subcellular DNA and RNA imaging are pushing the boundaries of spatially resolved single-cell biology, a comparable technology for mapping single proteins is still missing. To achieve a comprehensive understanding of protein organization at the nanoscale, four critical challenges must be addressed: sensitivity, throughput, spatial resolution, and multiplexing capabilities.

Mass spectrometry-based proteomics is the leading method for protein quantification, offering multiplexing and throughput capabilities reaching up to 5,000 different proteins with single-cell resolution.[5] For attaining subcellular resolution, techniques like imaging mass spectrometry,[6] multiplexed ion beam imaging,[7] and CODEX[8] utilize the specific labeling of antibodies conjugated with metal ions or DNA, enabling subcellular profiling of tissue samples with up to 100 targets and a spatial resolution of up to 260 nm.

However, the size of most proteins lies in the 5–10 nm range. The investigation of protein arrangements has seen significant

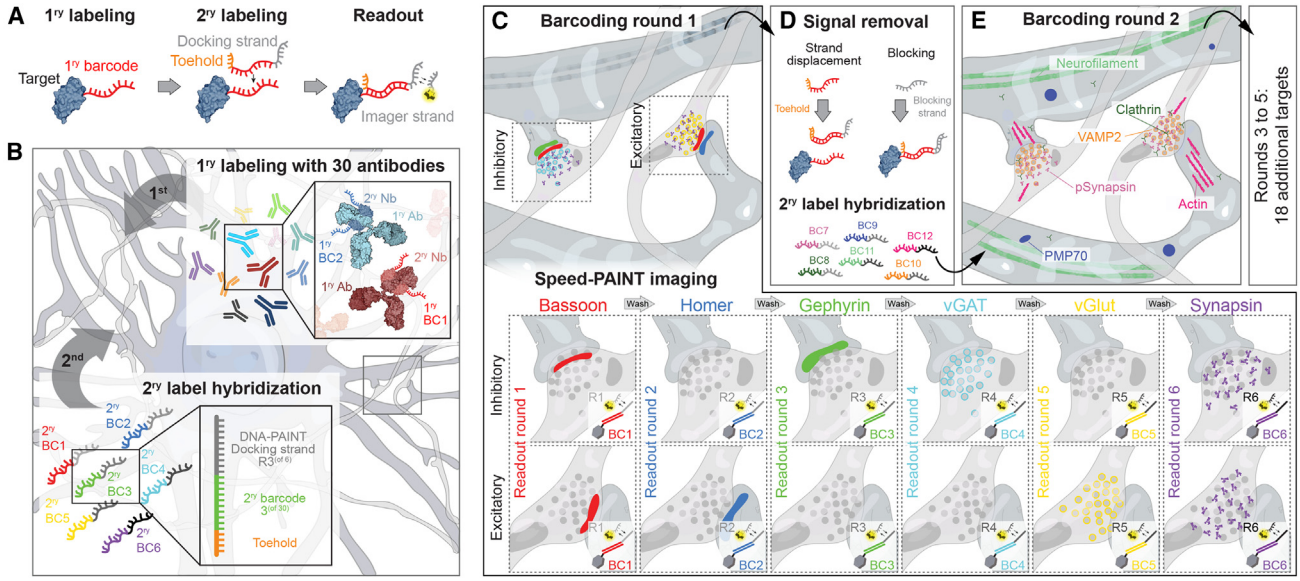

Figure 1. Secondary-label-based DNA-PAINT enables highly multiplexed imaging of single proteins

(A) Targets are labeled with a primary (1^{ry}) DNA barcode (red) and a secondary (2^{ry}) label composed of the full barcode complement sequence, a toehold (orange) and the speed-optimized DNA-PAINT docking sequences (gray). For readout, a complementary dye-labeled imager strand is added.

(B) Proteins are labeled by primary antibodies (Abs) preincubated with secondary nanobodies (Nbs), with a total labeling complex size of approximately 20 nm carrying the 1^{ry} barcodes. Subsequently, a subset of six 2^{ry} barcodes (BC1–BC6) carrying individual Speed-PAINT docking sequences (R1–R6) are hybridized to the respective 1^{ry} barcodes.

(C) Barcoding round 1 consists of six-target Exchange-PAINT imaging using speed-optimized sequences. In this instance, a subset of both excitatory and inhibitory pre- and post-synaptic proteins are targeted.

(D) Post-acquisition, 2^{ry} labels are inactivated by a combination of toehold-mediated strand displacement and docking strand blockage. Afterward, a new set of 2^{ry} barcodes (BC7–BC12) again carrying Speed-PAINT sequences (R1–R6) are introduced.

(E) Barcoding round 2 is then performed similarly to (C) and the whole procedure is repeated until all protein targets are acquired (30 targets in this schematic).

advancements through super-resolution microscopy.[9–11] Nonetheless, many of these techniques suffer from considerable limitations when it comes to highly multiplexed imaging.

DNA-PAINT is a super-resolution technique that relies on the transient binding of dye-labeled "imager" strands to their complementary "docking" strands present on target molecules of interest.[12,13] This approach facilitates conceptually unlimited multiplexing through sequential imaging, also known as Exchange-PAINT.[14–16] However, the throughput has traditionally been limited. Although approaches like FRET-based probes[17] or Fluorogenic DNA-PAINT[18] show improvements, optimized sequence design and repetitive sequence motifs improved DNA-PAINT's acquisition speed[19,20] by a factor of 100. However, this optimization reduces multiplexing to six targets.

Here, we introduce secondary label-based unlimited multiplexed PAINT (SUM-PAINT), a method capable of achieving virtually unlimited multiplexing while maintaining the throughput improvement offered by optimized sequence design. We achieved this unlimited multiplexing and throughput improvement by decoupling the DNA barcoding of the target from the imaging process using a primary barcode and a secondary label. We demonstrated this technique by generating hippocampal neuronal atlases by imaging up to 30 protein targets at single-protein resolution.

These atlases allowed us to adapt approaches from unsupervised machine learning and omics-inspired analysis for data exploration. With AI-guided analysis of the multiplexed protein content of almost 900 individual synapses, we uncovered a previously unreported potential third synapse class characterized by the juxtaposition of the postsynaptic scaffold of an inhibitory synapse combined with a presynaptic excitatory vesicle pool.

RESULTS

Secondary-label-based DNA-PAINT enables highly multiplexed imaging of single proteins

Requirements for achieving spatial proteomics at the single-protein level using super-resolution microscopy are high spatial resolution and multiplexing at adequate throughput, which is paramount for sufficient statistics. Although, for example, Exchange-PAINT[14] theoretically enables unlimited levels of multiplexing, throughput has been limited by slow association kinetics. Recent advancements in speed-optimized DNA-PAINT[19,20] have led to a 100-fold improvement in throughput by using optimized sequence motifs. However, these requirements limit multiplexing to six targets.

To overcome this, we decoupled target imaging from multiplexing using a primary barcode and a secondary label in an approach we call SUM-PAINT (Figure 1A). In this workflow, a primary target of interest is conjugated to a unique 20-nt long DNA sequence: the primary barcode. In a second step, a secondary label, containing a 20-nt complement to the primary barcode, is introduced. This secondary label also contains a

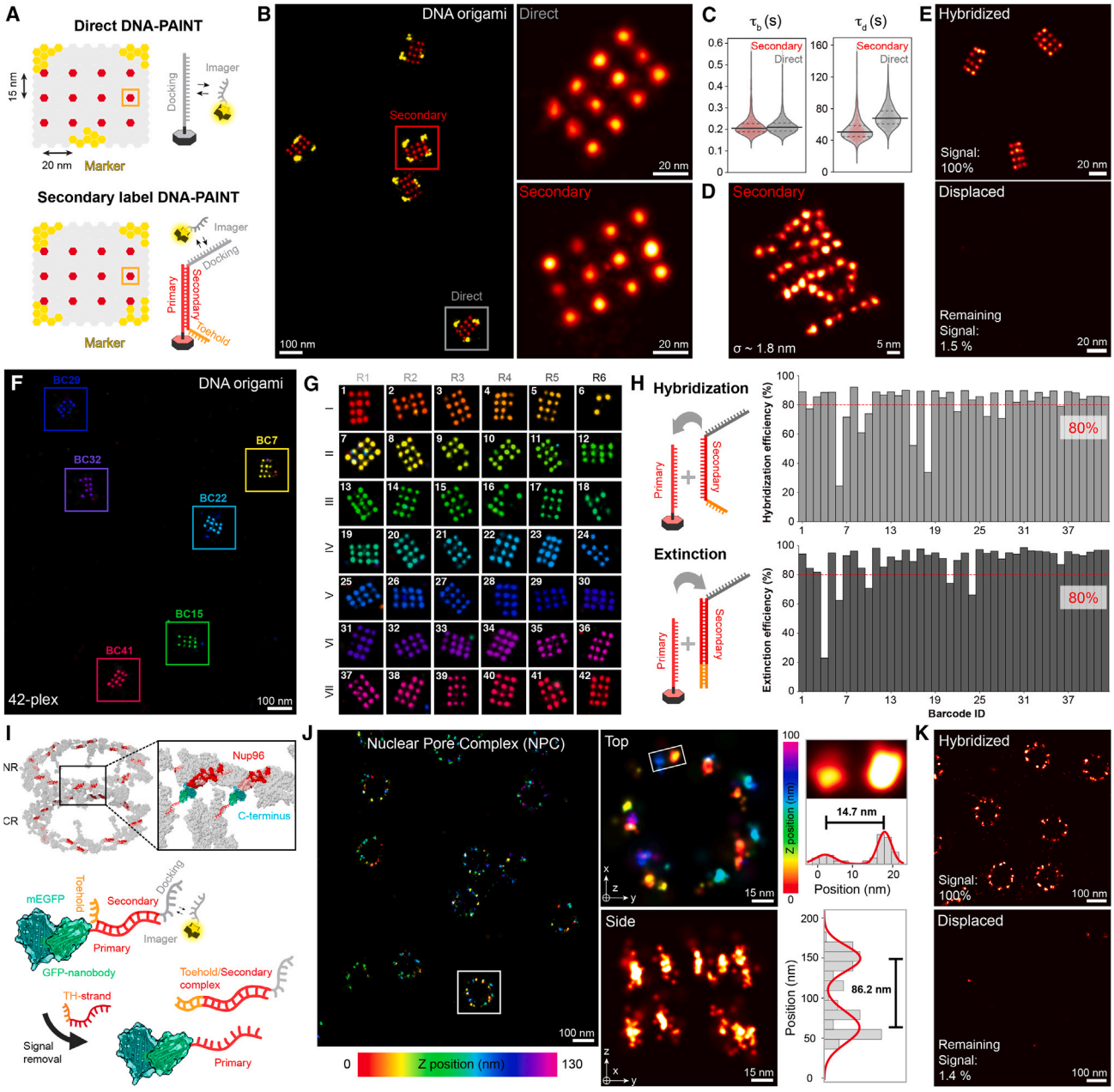

Figure 2. SUM-PAINT enables speed-optimized multiplexed imaging at sub-5-nm resolution

(A) Schematic representation of DNA origami structures used for benchmarking direct vs. secondary-label DNA-PAINT.

(B) Simultaneous acquisition of direct vs. secondary-label DNA-PAINT yields equivalent imaging performance (geometrical barcode (yellow) is acquired using Exchange-PAINT for structure identification).

(C) Binding kinetic comparison between direct and secondary-label DNA-PAINT shows similar bright times (τ_b), yet 30% shorter dark times (τ_d), yielding faster image acquisition.

(D) State-of-the-art sub-5-nm image resolution is demonstrated by resolving the 5-nm MPI logo on DNA origami.

(E) Using toehold-mediated strand-displacement, ~1.5% of the signal remains after displacement.

(F) A representative region of a 42-plex screening experiment showing six different 15-nm DNA origami grid structures, each carrying one out of 42 primary barcodes.

(G) Codebook for the 42-plex screening experiment with an exemplary DNA origami for each barcode, with columns representing barcoding rounds and rows imager-specific readout rounds.

(H) Hybridization efficiency (a combination of primary barcode incorporation and secondary label hybridization efficiency) for all 42 barcodes (top). Extinction efficiency (percentage of correctly displaced secondary labels) for all 42 barcodes (bottom).

(legend continued on next page)

speed-optimized docking sequence and a 10-nt long toehold for signal extinction via toehold-mediated strand displacement.[21] In the third step, dye-labeled, speed-optimized imager strands are added to visualize the target.

Sample preparation starts with the primary labeling step. Antibodies for each cellular target are preincubated with a secondary nanobody carrying a unique primary barcode. Secondary nanobody preincubation allows species-independent immunofluorescence.[22] Labeling of protein targets with these probes is then followed by a secondary hybridization step, where initially six secondary labels (each carrying one out of six available speed-optimized sequences) are hybridized to the respective primary barcodes (Figure 1B). Next, the six targets are sequentially read out using speed-optimized imager strands, as schematically shown for a target region containing different synapses (R1–R6, Figure 1C). After the first barcoding round is read out, the six secondary labels are removed (Figure 1D) for signal extinction. SUM-PAINT offers two possibilities for this extinction, which can be combined to achieve optimal performance: either the secondary label is removed via toehold-mediated strand displacement[21] or it is blocked via hybridization of a stable 19-nt complement to the DNA-PAINT docking sites. Following signal extinction, the next six secondary labels are hybridized, and the process is repeated until all 30 targets are imaged (Figure 1E). We note that signal removal by toehold-mediated strand displacement or blocking is a gentler approach to signal extinction compared to other sequential multiplexing techniques, which depend on the use of denaturation reagents.[23]

SUM-PAINT enables speed-optimized multiplexed imaging at sub-5-nm resolution

To apply SUM-PAINT in highly multiplexed, proteome-scale imaging experiments, we benchmarked its performance concerning spatial resolution, binding kinetics, and signal extinction efficiency. We first used DNA origami to assess SUM-PAINT's performance. We assembled two DNA origami, each containing 12 binding sites arranged in a 20 nm × 15 nm grid (Figure 2A; Table S1). The first nanostructure carried direct DNA-PAINT docking strands, while the second featured primary barcodes to which secondary labels were subsequently hybridized. Both structures were then simultaneously imaged using the same DNA-PAINT imager strand, followed by a second Exchange-PAINT imaging round for barcode-based structure identification (Figure 2A, yellow sites). Figure 2B represents an exemplary region with two zoom-ins, displaying one direct and one secondary label-extended structure. In both cases, single sites are resolved. A quantitative comparison of the binding kinetics (n = 400 structures) demonstrates that the secondary-label-based DNA-PAINT structures exhibit similar bright times (τ_b), but show a 30% shorter dark time (τ_d) possibly due to improved accessibility[24] (Figure 2C).

Next, we evaluated labeling efficiency (Figure S1A), defined as detected over designed number of binding sites. In DNA origami, one would expect to detect ~85% of the designed binding sites due to limitations in strand incorporation efficiency.[25] This implies that if we detect, for example, 85% labeling efficiency in our assay, actually 100% of the available sites are labeled. Subsequently, we tested the attainable spatial resolution of secondary-label-based DNA-PAINT and successfully resolved a 5 nm spaced "MPI" logo structure (Figure 2D), representing current state-of-the-art DNA-PAINT spatial resolution.[20,26]

To evaluate strand removal efficiency for signal extinction, we performed toehold-mediated displacement of the secondary label strand on DNA origami. Using an optimized hybridization buffer with 100 nM toehold probes, we achieved a signal extinction efficiency (defined as one minus the ratio of labeling efficiency before and after the extinction) >98% in less than 2 min (Figure 2E).

We then investigated SUM-PAINT's performance in sequential multiplexing. We designed 42 orthogonal DNA origami, each featuring a distinct primary barcode sequence (Table S1). Figure 2F shows an exemplary field of view of six DNA origami structures with unique barcodes. Figure 2G presents a gallery with a representative structure for each barcode.

From this 42-plex SUM-PAINT experiment, we assessed hybridization and signal extinction efficiency of secondary labels. We also used the "completeness" of the DNA origami to evaluate efficiency in both hybridization and signal extinction measurements (number of binding sites detected over the number of expected binding sites). Using this analysis, we determined hybridization efficiency to be ~80% and the average extinction efficiency to be ~89% (Figure 2H). Combining both metrics, we selected the best-performing barcodes for downstream experiments, with a hybridization efficiency >85% and extinction efficiency >93%. Again, considering that strand incorporation efficiency in DNA origami structures is ~85%, this yields an incorporation-adjusted hybridization efficiency of ~100%.

Finally, we performed cellular benchmarking using nuclear pore complexes (NPCs).[27,28] We focused on Nup96, which is present in eight pairs, exhibiting an 8-fold symmetry on both cytoplasmic and nuclear rings, totaling 32 copies. A homozygous Nup96-GFP knock-in cell line was used along with anti-GFP nanobodies conjugated to a primary sequence (Figure 2I). We then performed 3D imaging and successfully resolved Nup96 both laterally and axially at the expected distances (Figure 2J), yielding no significant difference between secondary-label-based and direct DNA-PAINT (Figure S1B).

Furthermore, we evaluated cellular extinction efficiency of secondary labels using toehold-mediated strand displacement. We found that compared to DNA origami, a longer displacement time was necessary for efficient strand removal, likely due to the more complex cellular sample environment. However, we could

(I) The Nuclear Pore Complex (NPC, PDB: 7PEQ) is used as a cellular benchmark for secondary-label DNA-PAINT. Nup96-GFP is labeled with DNA-conjugated anti-GFP nanobodies.
(J) Exemplary secondary-label 3D-DNA-PAINT overview image color-coded for height shows well-resolved NPC structures. Zoom-in of the highlighted NPC in the overview (top right) with cross-sectional histogram fit revealing well-resolved single Nup96 proteins at 14.7 nm distance. Side-view of the highlighted NPC in the overview with cross-sectional histogram fit reveals well-resolved nuclear and cytoplasmic parts of the NPC (bottom right).
(K) Using toehold-mediated strand-displacement, ~1.4% of the signal remains after displacement.

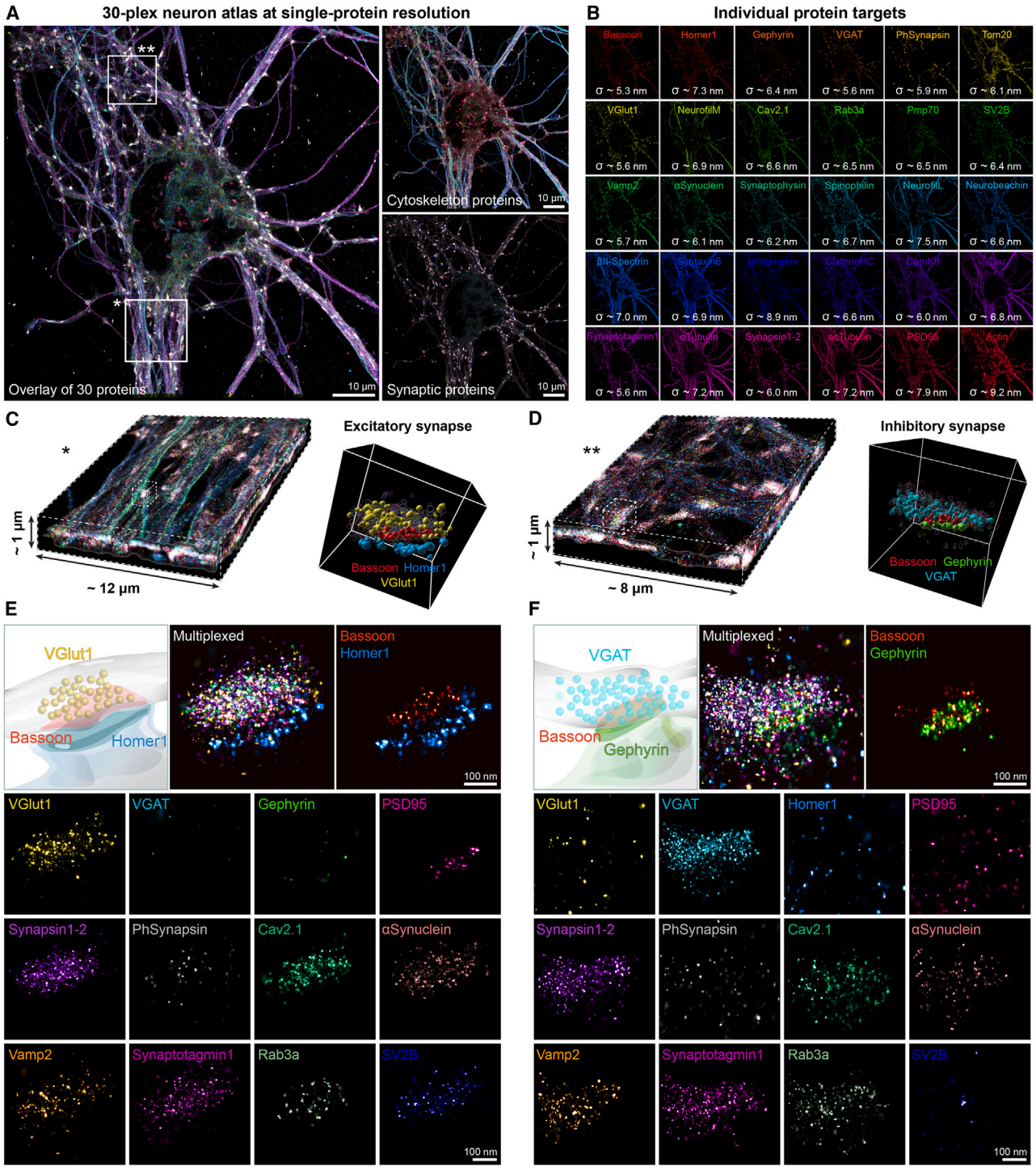

Figure 3. 30-plex neuron atlas at single-protein resolution

(A) Multiplexed SUM-PAINT overlay image of 30 protein targets visualized simultaneously in an individual neuron with single-protein resolution. Subsets of 9 cytoskeletal (top right) and 13 synaptic proteins (bottom right) from the same acquisition highlight specificity.

(B) 30 individual protein targets visualized separately with an average localization precision of 6.6 nm, calculated by nearest neighbor analysis.[29]

(C) 3D slice of one highlighted region from (A, bottom) alongside a zoom-in of a volume rendering of an individual excitatory synapse rotated *en-face* with the three key proteins Bassoon (red), Homer1 (azure), and VGlut1 (yellow) highlighted.

(D) 3D slice of the second highlighted region from (A, top) alongside a zoom-in of a volume rendering of an individual inhibitory synapse rotated *en-face* with the three key proteins Bassoon (red), Gephyrin (green), and VGAT (cyan) highlighted.

(legend continued on next page)

achieve an extinction efficiency (calculated as 1 minus the ratio of detected localizations in the extinction round vs. the detected localizations in the hybridization round) of ~98% after 15 min (Figure 2K). While toehold-mediated strand displacement proved highly efficient for signal extinction (Figures S1C and S1D), we additionally characterized the extinction efficiency through hybridization of a stable complement to the docking sequence. In both DNA origami and NPCs, this blocking achieves similar or even better performance (~99%) than strand displacement (Figures S1E and S1F). This flexibility enables us to choose between the two extinction methods or combine them for optimal performance.

30-Plex neuron atlas at single-protein resolution

Building a neuronal cell atlas with SUM-PAINT requires careful benchmarking of affinity reagents. We evaluated the performance of more than 100 binders using confocal and STED microscopy, followed by single-target DNA-PAINT. Pre-selected binders were then evaluated for SUM-PAINT multiplexing, yielding well-performing antibodies (see STAR Methods) for 30 target proteins (Table S2). One individual target imaging round in neurons takes ~17 min and yields an average localization precision of 6.6 nm, providing label-size-limited resolution. Adding time for hybridization and signal extinction, a 12-plex SUM-PAINT experiment is completed in less than 5 h (Figure S2). This represents a significant efficiency gain compared to classical Exchange-PAINT, which would require more than 300 h to achieve comparable spatial resolution and target sampling. While in theory, SUM-PAINT can be scaled to all 30 binders, the challenging neuronal environment requires a more complex staining procedure for higher multiplexing (see STAR Methods). Consequently, the total time required to construct a 30-plex neuronal atlas extends to approximately 30 h. Classical DNA-PAINT would require over 800 acquisition hours (more than a month), making this practically unfeasible.

Figure 3A shows the results of a 30-plex SUM-PAINT experiment, allowing us to map the super-resolved 3D protein distribution of 30 targets in a single neuron. Choosing two subsets of targets primarily localizing to the cytoskeleton or synapses (Figure 3A, right) highlights SUM-PAINT's specificity. SUM-PAINT shows specific, highest-resolution signals for each of the 30 proteins (Figures 3B and S3). To increase the signal extinction efficiency, we combined strand displacement with blocking for signal extinction, reducing the remaining post-extinction signal to <2% (Figure S4A).

As we acquire 3D data, we can analyze 3D protein distributions in synapses down to individual proteins. Figure 3C displays a 12 × 12 × 1 μm^3 imaging volume (region highlighted [*] in Figure 3A) along with a zoomed-in view of an excitatory synapse rotated *en-face*, revealing the composition of the presynaptic scaffold protein Bassoon (red), the excitatory postsynaptic scaffold protein Homer1 (azure), and the excitatory vesicular neurotransmitter transporter VGlut1 (yellow). Figure 3D presents an 8 × 8 × 1 μm^3 imaging volume (region highlighted [**] in Figure 3A) with a zoomed-in view of an inhibitory synapse, illustrating the nanoscale arrangement of Bassoon (red), the inhibitory postsynaptic scaffold Gephyrin (green), and the inhibitory vesicular neurotransmitter transporter VGAT (cyan). A comparison of the two selected synapses highlights, that specific markers for each synapse type, such as Homer1, VGlut1, and PSD95 for excitatory synapses, and Gephyrin and VGAT for inhibitory synapses, display signals exclusively in their respective types (Figures 3E and 3F).

Multiplexed SUM-PAINT provides nanoscale insights into neuronal architecture

Next, we benchmarked secondary-label-based DNA-PAINT on previously studied structures, analyzing the organization of the cytoskeletal protein Spectrin (βII-Spectrin) and the mitochondrial outer membrane marker Tom20 (Figure 4A). Figure 4B displays a magnified view of the periodic ring-like arrangement of Spectrin, along with an intensity projection. Subsequent Fourier transform and autocorrelation analysis revealed 190 nm ring-to-ring distance.[30] Tom20 localizations revealed the 3D architecture of the mitochondrial outer membrane with individually resolved proteins (Figure 4C). Figure 4D shows a representative region focusing on Clathrin heavy chain (ClathrinHC) alongside acetylated tubulin (ac-Tubulin). A closer examination of a single vesicle unveils the circular arrangement of individual proteins forming a spheroid. By aggregating the localizations of more than 200 individual vesicles and fitting the intensity maxima of the cross-section of the rings with a two-component Gaussian function, we determined an average diameter of ~60 nm for the Clathrin-coated pits.

Figure 4E shows Clathrin alongside the active zone, the postsynaptic density, and synaptic vesicles with an exemplary image of an excitatory synapse with prominent endocytosis occurring in a 5-plex overlay. An *en-face* arrangement of volumetric surface-rendered localizations revealed two Clathrin vesicles in the presynapse and most Clathrin vesicles in the postsynapse, as indicated by the position of the scaffold proteins Bassoon and Homer1 and the excitatory vesicle pool marker VGlut1. By rotating the synapse, we extracted a single Clathrin vesicle from the postsynapse, measuring ~100 nm in size.

To further explore the neuronal nanoarchitecture, we examined the previously observed assembly[32] of pre- and postsynaptic scaffolds into *trans*-synaptic nanocolumns (Figure 4F). We observed juxtaposed localization clusters ranging from 50 nm–100 nm in the pre- and postsynaptic scaffolds, illustrating the nanocolumnar substructure of adjacent scaffolds (Figure 4G). Since DNA-PAINT provides single-protein resolution, we took a closer look at these structures by rotating the scaffold to observe the alignment of individual nanocolumns (Figures 4H–4J). We then visualized neurofilaments with a focus on the light and medium chains. This structure was first observed in our multiplexed datasets, and we applied a subsequent secondary-label-based

(E) The exemplary excitatory synapse from (C) is visualized with all synaptic protein targets in a merged multiplexed view, followed by the scaffold proteins Homer1 and Bassoon as well as all protein targets separately.
(F) The exemplary inhibitory synapse from (D) is visualized with all synaptic protein targets in a multiplexed view, followed by the scaffold proteins Gephyrin and Bassoon as well as all protein targets separately.

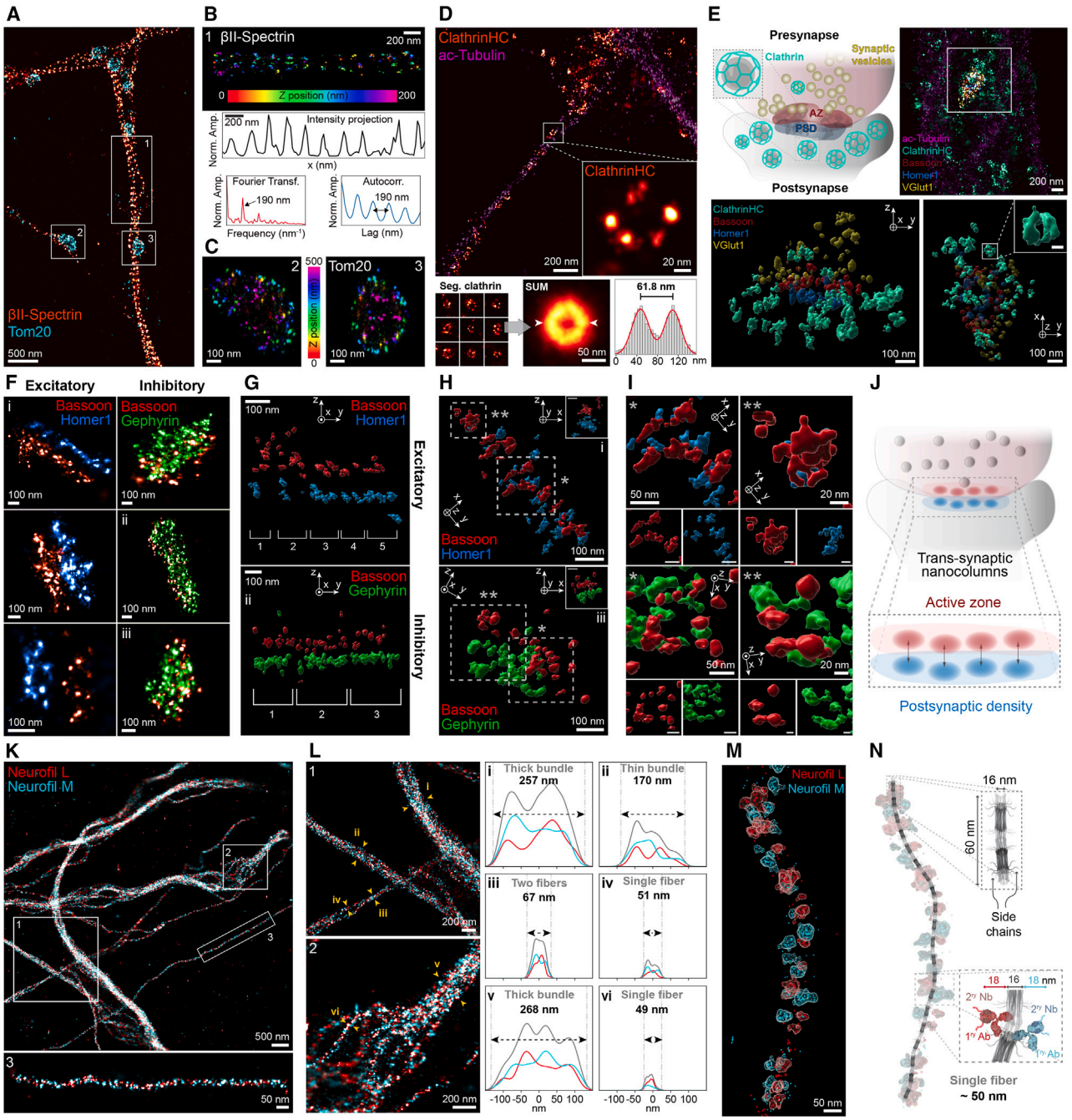

Figure 4. Multiplexed SUM-PAINT reveals nanoscale insights into neuronal architecture

(A) 2-plex overlay reveals periodic arrangement of Spectrin (βII-Spectrin, hot look-up table) alongside mitochondria (Tom20, cyan).

(B) Zoom into the selected Spectrin region from (A), color-coded for height. Cross-sectional histogram alongside autocorrelation and Fourier analysis confirms the periodic arrangement of well-resolved Spectrin rings at 190 nm spacing.

(C) Zoom into highlighted mitochondria from (A) reveals single Tom20 molecules (color indicates height).

(D) 2-plex overview of Clathrin alongside acetylated tubulin (ac-Tubulin) as cytoskeleton marker. Zoom-in shows a single traveling vesicle with individual Clathrin proteins resolved. Summing of single Clathrin vesicles and cross-sectional analysis of the sum image reveals an average diameter of ~60 nm.(E) Top left illustrates a synapse with prominent endocytosis occurring as shown by Clathrin vesicles (mint) present in both pre- and post-synapse alongside the Active Zone (AZ) in red, postsynaptic density (PSD) in blue, and synaptic vesicles in yellow. Top right shows a 5-plex image of a representative excitatory synapse, with Bassoon and VGlut1 on the presynaptic site and Homer1 on the postsynaptic site. Bottom shows the synapse in volumetric surface rendering in two rotated views, revealing spherical Clathrin vesicles (Scale bar: 50 nm).

(F) Exemplary excitatory and inhibitory synapses showing spatial correlation between pre- and postsynaptic scaffolds.

(legend continued on next page)

experiment to focus on details. Figure 4K shows an exemplary 2-plex composition of the light and medium chains, with a zoom-in on a single fiber at single-protein resolution, suggesting intertwined polymers. We further demonstrated that individual fibers are organized into bundles of varying thickness and assembled into higher-order structures containing up to eight individual fibers (Figure 4L). A cross-sectional profile of selected regions revealed that both the individual fiber width of approximately 50 nm and the thickest bundle width of approximately 260 nm appeared to be well conserved throughout the sample. Figure 4M shows most likely an individual fiber, ~50 nm thick, which aligns well with EM-derived measurements[31] of 16 nm, given the overall size of our labeling probe complex of approximately 18 nm (Figure 4N). This is further supported by the fact that the thickness of two fibers increased by 16 nm compared to a single fiber.

Unsupervised machine learning applied to spatial proteomics at single-protein resolution reveals a distinct synapse type

We then investigated the composition of synapses, which are key for proper brain function, and their complexity has not been explored at this level of resolution and multiplexing. With an atlas of 30 protein species in six independent datasets (Figure S4B), our aim was to uncover details of protein compositions and diversity.

We used uniform manifold approximation and projection (UMAP),[33] a nonlinear dimensionality reduction designed to preserve local and global structure of the data extensively used in biological applications.[34–36] However, SUM-PAINT advances this by employing single-protein-resolved super-resolution imaging, enriching the parameter space with morphometric features and 3D nanoscale mapping of biomolecules, assessing shape, density, protein count, and spatial cluster analysis for detailed surface, volume, and protein species correlations. To effectively use the SUM-PAINT feature space, we developed an integrated workflow for examining highly multiplexed super-resolution data (see STAR Methods). Figure 5A outlines our approach to data extraction and analysis. Initially, individual synapses were selected. Subsequently, 1,590 unique features (Table S4) were extracted by generating 3D histograms of the protein channels, followed by a DBSCAN spatial cluster analysis. Ultimately, we consolidated all features into a UMAP, followed by feature-space clustering using K-means[37,38] (Figure 5B).

This analysis identified three major clusters, beyond the conventional distinction between excitatory and inhibitory synapses. To investigate this "unexpected" type, we color-coded the UMAP based on expression levels of key proteins determining inhibitory and excitatory synapses: Bassoon as a general presynaptic scaffold, Gephyrin as an inhibitory postsynaptic scaffold, Homer1 as an excitatory postsynaptic scaffold, VGlut1 as a transporter for the excitatory neurotransmitter (glutamate), and VGAT as a transporter for the inhibitory neurotransmitter (γ-aminobutyric acid; GABA).

Furthermore, we traced back synapses from the UMAP analysis and visually examined protein composition for exemplary synapses (Figure 5B, red) in all channels corresponding to different protein types. As an example, by visualizing the protein content, we concluded that synapses expressing Homer1 and VGlut1 (e.g., synapse 59 and 60) are excitatory, while synapses expressing Gephyrin and VGAT (e.g., synapse 120 and 139) are inhibitory.

Interestingly, the synapse with identification number 138 belongs to an unreported type, which we define as "mixed": characterized by VGlut1 as a neurotransmitter vesicular transporter, originating from a glutamatergic neuron, but coupled with a postsynapse expressing Gephyrin as a scaffold protein.

Next, we visualized synapse 138 using volumetric surface rendering and examined protein composition of this "mixed" synapse by rendering each protein channel individually (Figure 5C). There was no significant signal for either Homer1 or VGAT, while both Gephyrin and VGlut1 displayed clearly defined spatial protein clusters, aligning with the synapse morphology at the nanoscale level. By analyzing all datasets, we deduced that mixed synapses are characterized by concomitant positive signals in the VGlut1 and Gephyrin channels and absence of Homer1 (Figure S5A). We furthermore studied the abundance of the mixed synapses with higher throughput by two-color STED microscopy, which allowed us to characterize over 4,500 synaptic puncta (Figure 5D). Analysis of these puncta in culture revealed that ~6% were of the mixed type. To corroborate our findings, we measured their percentage in brain slices from the stratum radiatum of the CA1 region of the hippocampus in P50 mice (Figure S5B). Here we confirmed the low abundance (~1.3% in this region) of mixed synapses, which might explain why they were not previously observed.

For further characterization, we evaluated developmental influences on synapse numbers within our culture model (Figure S5C), as well as the distribution of different neurotransmitter receptors (Figure S5D). These experiments indicated that, while

(G) Excitatory and inhibitory scaffolds rotated *en-face* and shown as volumetric surface rendering reveal the molecular arrangement of pre- and postsynaptic scaffolds into nano-pillars. (**i** and **ii** correspond to **i** and **ii** in F).

(H and I) Close-ups and rotations of excitatory and inhibitory synapses (**i**) and (**iii**) from (F).

(J) Schematic illustration of *trans*-synaptic nanocolumns highlighting corresponding clusters for the active zone and postsynaptic density involved in signal transduction.

(K) 2-plex overlay of intermediate neuronal filaments (medium (M) and light (L) chain in cyan and red respectively). Zoom-in shows a selected individual filament with alternating medium and light chains (bottom).

(L) Two exemplary selections indicating the arrangement of neurofilament into different strength bundles. Top shows a selection of different thicknesses, while bottom shows the organization of 8 individual filaments into a thick bundle. Line profiles of respective filaments (**i-vi**), with respective thicknesses conserved across the sample.

(M) Zoom-in of an individual fiber rendered as localizations and volumetric surface, showing individual protein molecules.

(N) Illustration of the proposed neurofilament structure from electron microscopy (EM)[31] labeled with antibodies. Two antibodies with an average size of 18 nm in addition to the 16 nm filament size result in an approx. 50 nm fiber. Remarkably, the single and two fibers from (L) are consistent with the thickness measured by EM.

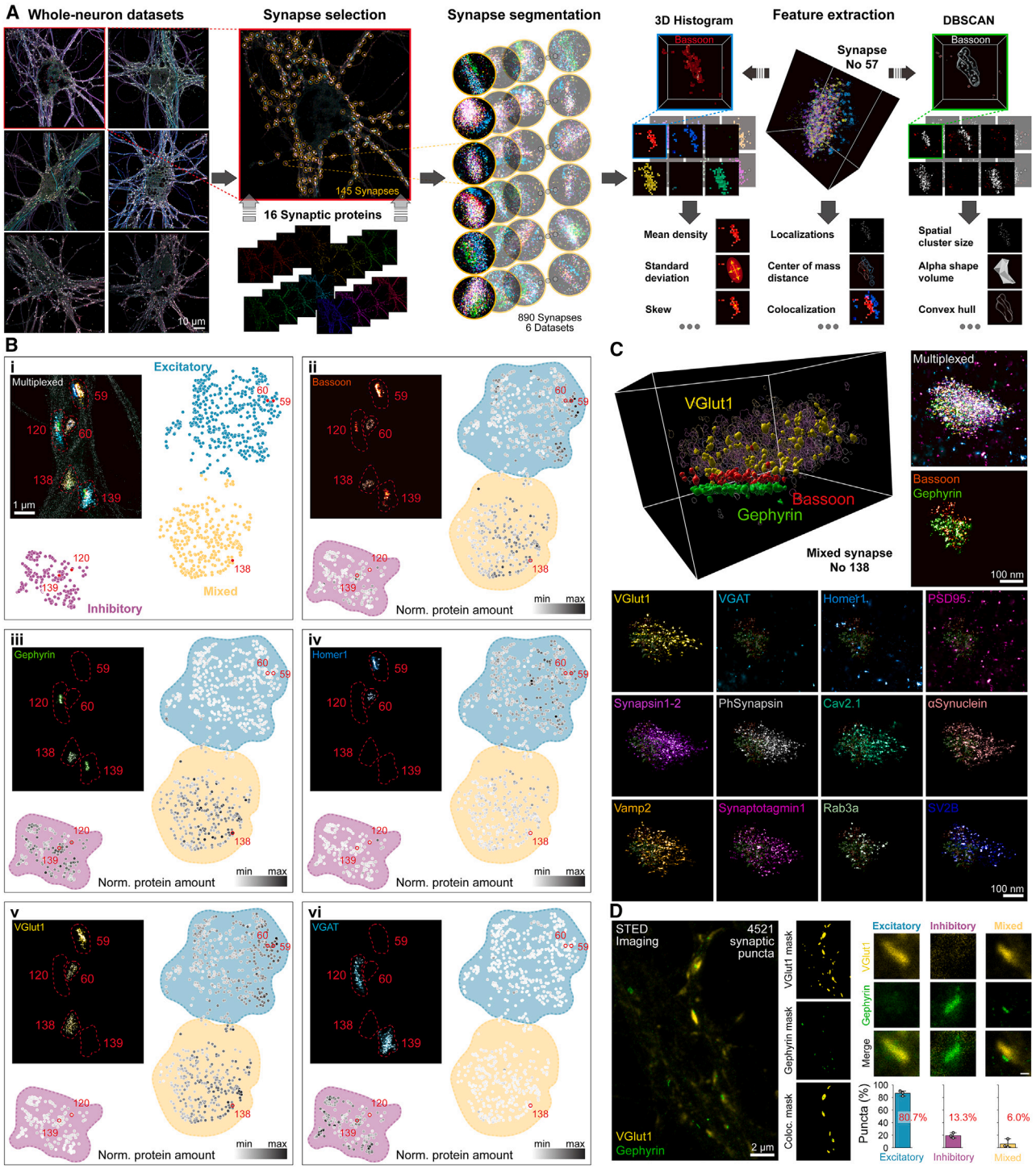

Figure 5. Unsupervised machine learning applied to spatial proteomics at single-protein resolution reveals a distinct synapse type

(A) Feature extraction workflow of six multiplexed whole-neuron datasets. In total 890 synapses are segmented from a 16-plex overlay of synaptic proteins. The localizations in the segmented synapses are analyzed as 3D histograms and DBSCAN spatial clustering for parameter extraction, resulting in 1590 features per synapse.

(B) A UMAP of 1590 features is created and clustered (i), yielding three populations of synapses. The individual synapses are labeled with their identification number from the analysis workflow and are highlighted in the UMAP. The top left shows the multiplexed overlay of excitatory and inhibitory markers alongside ac-Tubulin (dark green background) as cytoskeleton reference. The unique composition of pre- and postsynaptic markers (Bassoon, Homer1, Gephyrin), as well as

(legend continued on next page)

the total number of VGlut1 positive and Gephyrin positive synaptic clusters increases during development, the number of mixed synapses remains constant. Moreover, we observed that the postsynaptic receptors are, in 80% of the cases, of the GABAAγ2 type and only ~10% show a positive signal for GluA (Figure S5D). This suggests that the majority of mixed synapses have inhibitory postsynaptic receptors, and future studies will clarify whether the remaining ~10% have different types of receptors. Finally, we examined the recycling ability of synaptic vesicles in the three synapse types and confirmed that synaptic vesicles in the mixed type recycle similarly to excitatory synapses (Figure S5E), as expected from their predominant excitatory presynaptic molecular composition.

High-content feature space analysis enables deep investigation of synapse type characteristics revealing synaptic diversity

To delve deeper into synaptic features, we analyzed all synaptic proteins (Figures 6A and S6). In addition to the pre- (Bassoon) and postsynaptic scaffold proteins (PSS: Homer1, Gephyrin) and neurotransmitter transporter proteins (NTT: VGlut1, VGAT), the analysis also incorporates several synaptic vesicle and vesicle pool proteins (Synaptotagmin1, Rab3a, Vamp2, SV2B), vesicle pool associated proteins (Synapsin, Phospho-Synapsin, α-Synuclein), and the calcium channel protein Cav2.1 (Figure 6B). Our analysis workflow focused on the following points: i) Center of Mass (CoM) position for each protein localization cluster (yielding average distances between synaptic protein distributions), ii) Relative protein amount and cluster volume for each species (revealing protein abundance for different synapse types and the actual volume of the protein distributions), iii) Spatial profile example within the synapse types (serving as a visual reference), iv) Volume correlation and subsequent hierarchical clustering between protein species (enabling a comparison of expression levels among different protein species and synapse types).

Comparing CoM distances between protein species enabled us to extract metrics such as colocalization and average distance. We represented the CoM distance between all proteins (obtained from an average of 890 synapses) in a 9x9 matrix, highlighting the synapse-specific proteins (PSS and NTT) as individual values (Figure 6C). Our analysis yielded, for example, a distance of 136 nm between Bassoon and PSS, in good agreement with earlier studies.[39,40] Furthermore, the CoM analysis of vesicle pool proteins toward each other reveals closer distances in the range of 50–80 nm. Given micron-sized vesicle pools, this indicates colocalization of protein clusters. For an even more detailed analysis, we calculated the CoM distances for individual types of synapses in Figure S6A.

Next, we evaluated the relative protein amounts and volume for each synapse type (Figure 6D). The matrix displaying relative protein amounts replicates the distributions between PSS and NTT observed from the normalized protein amount UMAP analysis in Figure 5B, with excitatory synapses displaying Homer1 and VGlut1, inhibitory Gephyrin and VGAT, and mixed Gephyrin and VGlut1. Additionally, we can infer that the common vesicle pool proteins (Synaptotagmin1, Rab3a, and Vamp2) exhibit similar expression levels, whereas Synapsin, PhSynapsin, SV2B, and α-Synuclein are lower expressed in inhibitory synapses. Pre- and postsynaptic scaffolds have a volume of ~0.05 μm^3, while the vesicle pool proteins form a much larger structure with volumes of ~0.3 μm^3.

While the relative protein amount can provide valuable information, this feature can only be compared within a specific protein species (e.g., between different synapse types) but not between different protein species. This is because different labeling efficiencies of antibodies lead to substantial variations in the number of localizations for each protein target, which is not calibrated in our current study. To be able to make quantitative conclusions between all synaptic protein species we transitioned to a more globally comparable feature such as the protein cluster volume, which is less influenced by labeling efficiencies. To acquire information about protein expression levels, we used a metric that we call relative volume ratio, which is the ratio between the volume of one protein species and another in the same synapse.

The top panels of Figures 6E–6G presents an exemplary image of an individual synapse for each synapse type, alongside its protein localization profiles as violin plots (spatial profile). Protein species that show no clusters in the respective synapse are not used in the volume analysis. The profile recapitulates that pre- and postsynaptic scaffolds for all three synaptic subtypes are spaced approximately 150 nm apart on the level of individual exemplary synapses.

After the volume is detected by DBSCAN clustering, we calculated the relative volume ratio between all protein species in each synapse. To extract correlations between the protein volumes, we used a Pearson correlation plot. Figure S6D shows a few examples for this analysis indicating strong correlation between the abundance of for example Synaptotagmin1 and the NTT among all three synaptic subtypes. To make this more accessible, we individually summarized them in an 11x11 matrix for each synaptic subtype (Figures 6E–6G, middle). These correlation matrices reveal substantial differences between excitatory and inhibitory synapses.

For more quantification, we employed hierarchical clustering to construct a dendrogram illustrating the similarity clusters of protein species (Figures 6E and 6F, bottom). Pre- and postsynaptic scaffold proteins (Bassoon and PSS, respectively) exhibit a strong correlation for both excitatory and inhibitory synapses, as do the common vesicle pool proteins Synaptotagmin1,

the neurotransmitter transporter (VGlut1, VGAT) allows us to label the UMAP clusters as excitatory (blue), inhibitory (purple) and a distinct mixed synaptic population (yellow). (ii–vi) highlights the normalized protein content (grayscale) of a single pre- or postsynaptic marker in the UMAP. The top left shows a single channel image of the same region for each protein.

(C) Volumetric surface rendering of a mixed synapse rotated *en-face* (top left), containing VGlut1 as a neurotransmitter transporter, Bassoon as presynaptic, and Gephyrin as postsynaptic marker. Top right represents the same synapse in a 13-plex overlay and as a 2-plex image containing Bassoon and Gephyrin. The bottom shows 12 additional protein channels at single-protein resolution.

(D) High-throughput STED imaging of more than 4520 synaptic puncta indicates that the relative abundance of the mixed synapse type is 6%.

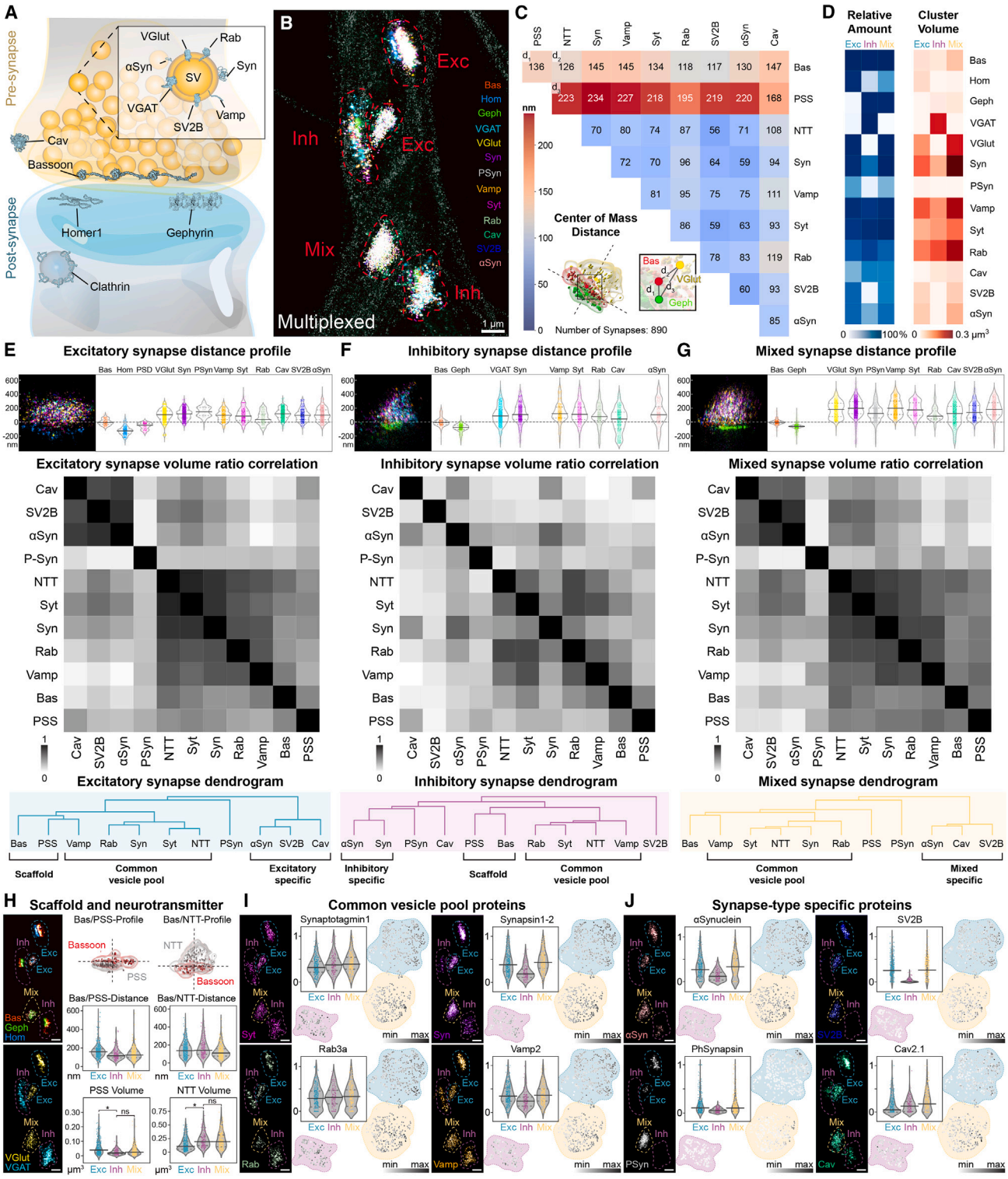

Figure 6. High-content feature space analysis enables deep characterization of synaptic diversity

In this figure protein names were abbreviated as: Bassoon:Bas, Homer1:Hom, VGlut1:VGlut, Synapsin1-2:Syn, PhSynapsin:PSyn, Vamp2:Vamp, Synaptotagmin1:Syt, Rab3a:Rab, Cav2.1:Cav, α-Synuclein:αSyn, Gephyrin:Geph.

(A) Schematic illustration of synaptic proteins included in the high-content analysis. Note that for representation purposes VGlut1 and VGAT as well as Homer1 and Gephyrin are shown in the same scheme.

(legend continued on next page)

Rab3a, Vamp2, and the NTT. Interestingly, in excitatory synapses, Synapsin shows high correlation with other vesicle pool proteins, while for inhibitory synapses, it exhibits a strong correlation with α-Synuclein, forming an inhibitory-specific cluster. Notably, α-Synuclein, SV2B, and Cav2.1 display a pronounced correlation cluster in excitatory synapses, while no correlation is observed in the inhibitory case, making it an excitatory-specific cluster. Phosphorylation of Synapsin at site 6 (Ser549), which we term PhSynapsin, does not correlate with any other protein, indicating that future more detailed studies of post translational modifications will broaden our knowledge about synaptic diversity.

We then compared the volume ratio correlation matrix and dendrogram of the mixed to those of excitatory and inhibitory synapses (Figure 6G, middle and bottom). The mixed type exhibits greater similarity to excitatory synapses than inhibitory ones.

While the volume correlation analysis between proteins among the three synaptic subtypes highlights the similarity between excitatory and mixed synapses and the difference with inhibitory synapses on a global scale, our feature space allows to investigate more general characteristics of the three populations in detail, such as similarity clusters we obtained after hierarchical clustering (Scaffold, common vesicle proteins, synapse type specific) across types. First, we focused on differences in PSS and NTT between the synapse types by analyzing the volume and distance between the pre- and postsynaptic scaffold and between the presynaptic scaffold and NTT (Figure 6H). The CoM distance comparison plot for the individual synapse types reveals that the distance between vesicles and either pre- or postsynaptic scaffolds depends on the respective PSS. The volumetric comparison between the PSS of three subtypes also indicates that excitatory Homer1 PSS differs in size from the conserved inhibitory and mixed Gephyrin PSS size. Although NTTs vary from excitatory to inhibitory synapses, the distance between Bassoon and NTT appears conserved. However, the NTT volume, which approximates the size of the synaptic vesicle pool for each synapse, seems to be correlated with the PSS identity, with the excitatory VGlut1 exhibiting a smaller volume than VGAT or VGlut1 in either inhibitory or mixed synapses.

Finally, we explored how the common vesicle proteins and the synapse type specific correlation clusters resulting from the dendrogram differ on a single-synapse level. We display the expression level of the given proteins as violin plots showing the population average as well as the intensity-colored UMAP, indicating the expression difference on a single synapse level. This expression difference can be further investigated in an exemplary region of the imaging data. Our initial target was the distribution of common vesicle pool proteins Synaptotagmin1, Rab3a, Vamp2, and Synapsin. Figure 6I reveals that Synaptotagmin1 and Rab3a are evenly distributed among all three synapse subtypes. Interestingly, Vamp2 and Synapsin show a difference in inhibitory synapses. While Vamp2 is slightly lower expressed in inhibitory synapses, Synapsin exhibits a much lower expression level in both the average overall synapses and the UMAP, where each synapse is shown individually. The lower expression level of Synapsin has been reported before,[41] and our pipeline replicates this finding.

Our further analysis focused on the synapse-type-specific protein correlation clusters, which indicated a significant difference between synapse subtypes. Figure 6J shows that α-Synuclein is strongly downregulated in the inhibitory synapses, consistent with previous reports.[42] SV2B exhibits almost no signal in inhibitory synapses, as previously reported.[43,44] Moving on to PhSynapsin and Cav2.1, we observed that phosphorylation of Ser549 is only occurring at excitatory and mixed synapses. Furthermore, Ser549 phosphorylation on Synapsin in these synapse types is a distinct event, suggesting an orthogonal level of regulation, as indicated by a strong difference in the UMAP intensity color for individual synapses. While present in all synaptic subtypes Cav2.1 expression is lower in excitatory synapses and also displays a high expression level variability in the UMAP.

DISCUSSION

With SUM-PAINT, we pioneered a method to advance super-resolution imaging, achieving high spatial resolution and throughput for a virtually unlimited number of protein targets. By developing an analysis workflow that incorporates machine learning and omics-inspired approaches, we obtained highly multiplexed, high-resolution datasets and zoomed into individual sample regions to reveal nano-arrangements down to single proteins. Applying SUM-PAINT to neurons, we generated the most

(B) Multiplexed super-resolution overlay of 13 synaptic proteins under investigation.
(C) Average center-of-mass (CoM) distance matrix of 890 synapses alongside illustration of CoM analysis of three exemplary synaptic proteins with respective distances d_1, d_2, and d_3 (bottom left).
(D) Left: Heatmap of the normalized relative protein counts for each protein type for excitatory, inhibitory and mixed synapses. Right: Protein cluster volume (in μm^3) for each protein type for excitatory, inhibitory and mixed synapses.
(E) Top: Exemplary excitatory synapse localization distribution after DBSCAN spatial cluster detection. Center: Heatmap of the Pearson correlation coefficients of the protein volume ratios. Bottom: Dendrogram resulting from a hierarchical cluster analysis of the volume ratio correlation of all synaptic proteins.
(F) Same as (E) for inhibitory synapse type.
(G) Same as (E) for mixed synapse type.
(H) Analysis details for scaffold and neurotransmitter transporter (NTT) proteins. Top left shows a 3-plex composition of scaffold proteins with the synapse type indicated. Bottom left shows the respective region for the NTT. Top middle and right show an exemplary profile of the presynaptic scaffold protein Bassoon (Bas) to the postsynaptic scaffold (PSS) (middle) and NTT (right) with volumetric rendering. Center middle and right show the synapse type specific CoM distance for Bas to the PSS (middle) and to the NTT (right). Bottom middle and right show the synapse type-specific protein volume of PSS and NTT. * indicates p value < 0.05.
(I) Analysis details for the common vesicle pool proteins. Top left shows the individual imaging result for Synaptotagmin1 of the selected region alongside a synapse type specific violin plot, showing the average of the relative normalized protein content and a UMAP with the protein content colored in grayscale. While the violin plot highlights the average value of the protein content among the different synapse species, the UMAP also indicated the difference in individual synapses. Top right, bottom left and right display the same arrangement for Synapsin1-2, Rab3a and Vamp2.
(J) Analysis details of synapse type-specific proteins. Same as (I) for α-Synuclein, SV2B, Phospho-Synapsin (PhSynapsin) and Cav2.1.

extensive multiprotein dataset to date, comprising up to 30 distinct protein targets in parallel with an average localization precision of 6.6 nm. These multiplexed neuronal architecture maps allowed to resolve synapses with high spatial resolution and open the field to the possibility of analyzing synaptic and even subsynaptic variability in response to plasticity modulations.

To our knowledge, our work is the most comprehensive spatial study to date of the molecular diversity of synapses combining information of protein identity and detailed morphometric features. Considering this diverse feature space for multiple proteins in parallel, our analysis workflow allows a comprehensive investigation of synapse diversity. Through our AI-guided analysis, we unveiled three distinct synaptic subtypes within hippocampal neurons: canonical glutamatergic excitatory and GABAergic inhibitory synapses, and a mixed synaptic subtype. This unexpected mixed subtype contains an excitatory glutamatergic synaptic vesicle pool (VGlut1^{+}) paired to a Gephyrin-positive postsynaptic scaffold, typically associated with inhibitory synapses. Given that Gephyrin, should not directly cluster with glutamatergic receptors (Figure S5D) it is probable that these synapses do not take part in traditional neurotransmission.

The discovery of this synapse subtype raises a number of additional questions that will form the basis of future research aimed at understanding their physiological significance, possible transient nature, and role in development and disease. As our data suggests a higher similarity between mixed and excitatory synapses, we hypothesize that these may represent synapses transitioning to a fully excitatory state upon refinement, possibly through an unknown series of steps.

Moreover, we were able to characterize the details of excitatory, inhibitory, and the newfound mixed synapses, leveraging several features such as interprotein cluster distances, shape and volume of protein distribution, as well as their correlation matrices. This analysis allowed us to decode the specifics of synaptic subtypes. Certain proteins, including α-Synuclein, SV2B, and Cav2.1, display varying correlations with different synaptic subtypes, and suggesting a differential role in human pathologies. In our exploratory studies, we employed a binder targeting phospho-Ser549 of Synapsin (PhSynapsin), a synaptic readout of MAP kinase activity, which illuminates variations in synaptic plasticity tied to local synaptic signaling and suggests potential functional state variations across synapses. Future investigations will help elucidate how signaling influences synaptic heterogeneity.

UMAP distributions (Figures 6I and 6J) show that different synaptic proteins exhibit "expression gradients" within different synaptic subtypes (i.e., unevenly distributed expression levels). This pattern may indicate a thus far poorly understood temporal evolution of synaptic identities, or alternatively hint at the existence of additional, yet-to-be-discovered subtypes amenable to targeted genetic or pharmacological interventions. Altogether, our findings underscore the nanoscale diversity of synaptic subtypes, transcending mere differences in molecular composition. Our work not only unveils a distinct synaptic connection subtype, but also implies uncharted diversity in the activity of individual synaptic contacts.

In this study, we focused on the analysis of a subset of features from our neuron cell atlases. However, the feature space can be expanded to examine any area of biological interest, such as density variations, similarities in protein distributions, or further categorization into characteristics like synaptic subtypes. Our integrated workflow for multiplexed protein nano-architecture exploration can be applied to any biological system with the goal of investigating potential interactions or molecular distributions of interest. SUM-PAINT enables hypothesis-free mapping of protein distributions and allows for unbiased feature extraction. Once interesting protein arrangements or correlations have been identified, a lower-plex experiment can be carried out, focusing on enhancing data statistics.

Despite our comprehensive analysis, we have only begun to tap into the wealth of potential investigations afforded by the datasets we have generated. In summary, we offer an integrated data acquisition and analysis workflow with unparalleled levels of multiplexing and spatial resolution, laying the groundwork for comprehensive spatial proteomics at single-protein resolution through localization microscopy.

Limitations of the study

As SUM-PAINT relies on affinity reagents, it is limited by their potential nonspecific binding and epitope clustering. We have devised blocking procedures to minimize nonspecific binding and implemented post-fixation steps to prevent probe unbinding. However, future advancements in developing smaller, more efficient primary binders will enhance SUM-PAINT's performance. Furthermore, for the application of SUM-PAINT, we have used primary neurons, which can recapitulate several aspects of neuronal development *in vitro,*[45,46] as these preparations provide optimal penetration of binders and minimal background. In these cells, we describe a previously unrecognized class of apparently mismatched chemical synapses that we refer to as "mixed", containing an excitatory presynaptic vesicle pool coupled to an inhibitory postsynaptic scaffold. Although we have observed similar mismatched synapses in adult mouse brain tissue, the physiological role and importance of mismatched synapses in brain physiology remains to be determined. Lastly, like all localization microscopy techniques, SUM-PAINT highlights the need for optical sectioning through selective plane illumination. While we currently can acquire single 1 μm planes, cells are several microns thick, and the elucidation of interconnections and the potential extension of this technique to tissue imaging will need approaches such as light-sheet microscopy.

STAR★METHODS

Detailed methods are provided in the online version of this paper and include the following:

- KEY RESOURCES TABLE
- RESOURCE AVAILABILITY
  - Lead contact
  - Materials availability
  - Data and code availability
- EXPERIMENTAL MODEL AND STUDY PARTICIPANT DETAILS
  - Animals
  - Primary cell culture

SUPPLEMENTAL INFORMATION

Supplemental information can be found online at https://doi.org/10.1016/j.cell.2024.02.045.

ACKNOWLEDGMENTS

We thank Isabelle Baudrexel, Eva-Maria Schentarra, Alexandra Eklund, Heinrich Grabmayr and Florian Schueder for helpful discussions and technical support.

This research was funded in part by the European Research Council through an ERC Consolidator Grant (ReceptorPAINT, Grant agreement number 101003275), the BMBF (Project IMAGINE, FKZ: 13N15990), the Max Planck Foundation, and the Max Planck Society.

S.S. acknowledges support by the QBM graduate school. E.U., S.C.M.R. and R.K. acknowledge support by the IMPRS-ML graduate school. L.A.M. and M.G. acknowledge a postdoctoral fellowships from the European Union's Horizon research and innovation program under the Marie Skłodowska-Curie grant agreement no. 101065980 (L.A.M.) and 796606 (M.G.). F.O. acknowledges support by Deutsche Forschungsgemeinschaft (DFG) through the SFB1286 (project Z04). E.F.F. is funded by a Schram Stiftung (T0287/35359/2020) and a Deutsche Forschungsgemeinschaft (DFG) grant (FO 1342/1-3). E.F.F. also acknowledges the support of the Collaborative Research Center 1286 on Quantitative Synaptologie (CRC/SFB1286), Göttingen, Germany. S.S.B has received funding from F. Hoffmann-La Roche (No grant number is applicable) and is supported by the Helmholtz Association under the joint research school 'Munich School for Data Science - MUDS'. C.M. has received funding from the ERC under the European Union's Horizon 2020 research and innovation program (Grant agreement No. 866411) and acknowledges support from the Hightech Agenda Bayern. Part of the schematics in Figures 1 and 4 were created with the help of Biorender (https://biorender.com). We thank Mark Browne (Andor Technology Ltd) for access to the Imaris software and NanoTag Biotechnologies as well as Synaptic Systems for providing us with free samples for antibody and nanobody testing.

AUTHOR CONTRIBUTIONS

E.M.U. developed the SUM-PAINT method, designed and conducted all DNA-PAINT and SUM-PAINT experiments, developed the spatial omics analysis workflow, analyzed and interpreted all data. S.S.B. developed the spatial omics analysis workflow, analyzed and interpreted synapse datasets. K.J. prepared neuron samples and performed antibody screening and STED imaging and analyzed data. L.A.M. analyzed and interpreted data. M.G. developed the SUM-PAINT method and performed initial experiments. Sh.S. prepared neuron samples and performed antibody screening. R.K. developed software and analyzed data. Se.S. prepared DNA-conjugated binders and performed initial experiments. S.C.M.R. developed software and analyzed data. A.P. prepared samples. C.M. supervised the spatial omics analysis workflow. F.O. supervised antibody screening, provided antibody and nanobody reagents, and interpreted data. E.F.F. supervised the neuron part of the study, prepared neuron samples, and analyzed and interpreted data. R.J. conceived the concept, designed experiments, interpreted data and supervised the study. E.M.U., L.A.M., E.F.F., and R.J. wrote the manuscript with contributions from all authors. E.M.U., S.S.B., and K.J. contributed equally. All authors reviewed and approved the final manuscript.

DECLARATION OF INTERESTS

E.M.U., M.G. and R.J. have filed a patent on the method published in this paper. F.O. is a shareholder of NanoTag Biotechnologies GmbH. The other authors declare no competing financial interests.

Received: May 17, 2023
Revised: November 28, 2023
Accepted: February 29, 2024
Published: March 28, 2024

REFERENCES

1. Chen, K.H., Boettiger, A.N., Moffitt, J.R., Wang, S., and Zhuang, X. (2015). RNA imaging. Spatially resolved, highly multiplexed RNA profiling in single cells. Science *348*, aaa6090.
2. Eng, C.-H.L., Lawson, M., Zhu, Q., Dries, R., Koulena, N., Takei, Y., Yun, J., Cronin, C., Karp, C., Yuan, G.C., and Cai, L. (2019). Transcriptome-scale super-resolved imaging in tissues by RNA seqFISH. Nature *568*, 235–239.
3. Allen, W.E., Blosser, T.R., Sullivan, Z.A., Dulac, C., and Zhuang, X. (2023). Molecular and spatial signatures of mouse brain aging at single-cell resolution. Cell *186*, 194–208.e18.
4. Takei, Y., Yun, J., Zheng, S., Ollikainen, N., Pierson, N., White, J., Shah, S., Thomassie, J., Suo, S., Eng, C.H.L., et al. (2021). Integrated spatial genomics reveals global architecture of single nuclei. Nature *590*, 344–350.
5. Mund, A., Coscia, F., Kriston, A., Hollandi, R., Kovács, F., Brunner, A.D., Migh, E., Schweizer, L., Santos, A., Bzorek, M., et al. (2022). Deep Visual Proteomics defines single-cell identity and heterogeneity. Nat. Biotechnol. *40*, 1231–1240.
6. Giesen, C., Wang, H.A.O., Schapiro, D., Zivanovic, N., Jacobs, A., Hattendorf, B., Schüffler, P.J., Grolimund, D., Buhmann, J.M., Brandt, S., et al. (2014). Highly multiplexed imaging of tumor tissues with subcellular resolution by mass cytometry. Nat. Methods *11*, 417–422.
7. Angelo, M., Bendall, S.C., Finck, R., Hale, M.B., Hitzman, C., Borowsky, A.D., Levenson, R.M., Lowe, J.B., Liu, S.D., Zhao, S., et al. (2014). Multiplexed ion beam imaging of human breast tumors. Nat. Med. *20*, 436–442.
8. Goltsev, Y., Samusik, N., Kennedy-Darling, J., Bhate, S., Hale, M., Vazquez, G., Black, S., and Nolan, G.P. (2018). Deep Profiling of Mouse Splenic Architecture with CODEX Multiplexed Imaging. Cell *174*, 968–981.e15.
9. Sahl, S.J., Hell, S.W., and Jakobs, S. (2017). Fluorescence nanoscopy in cell biology. Nat. Rev. Mol. Cell Biol. *18*, 685–701.

10. Sauer, M., and Heilemann, M. (2017). Single-Molecule Localization Microscopy in Eukaryotes. Chem. Rev. *117*, 7478–7509.
11. Lelek, M., Gyparaki, M.T., Beliu, G., Schueder, F., Griffié, J., Manley, S., Jungmann, R., Sauer, M., Lakadamyali, M., and Zimmer, C. (2021). Single-molecule localization microscopy. Nat. Rev. Methods Primers *1*, 39.
12. Jungmann, R., Steinhauer, C., Scheible, M., Kuzyk, A., Tinnefeld, P., and Simmel, F.C. (2010). Single-molecule kinetics and super-resolution microscopy by fluorescence imaging of transient binding on DNA origami. Nano Lett. *10*, 4756–4761.
13. Schnitzbauer, J., Strauss, M.T., Schlichthaerle, T., Schueder, F., and Jungmann, R. (2017). Super-resolution microscopy with DNA-PAINT. Nat. Protoc. *12*, 1198–1228.
14. Jungmann, R., Avendaño, M.S., Woehrstein, J.B., Dai, M., Shih, W.M., and Yin, P. (2014). Multiplexed 3D cellular super-resolution imaging with DNA-PAINT and Exchange-PAINT. Nat. Methods *11*, 313–318.
15. Wang, Y., Woehrstein, J.B., Donoghue, N., Dai, M., Avendaño, M.S., Schackmann, R.C., Zoeller, J.J., Wang, S.S.H., Tillberg, P.W., Park, D., et al. (2017). Rapid Sequential in Situ Multiplexing with DNA Exchange Imaging in Neuronal Cells and Tissues. Nano Lett. *17*, 6131–6139. https://doi.org/10.1021/acs.nanolett.7b02716.
16. Guo, S.-M., Veneziano, R., Gordonov, S., Li, L., Danielson, E., Perez de Arce, K., Park, D., Kulesa, A.B., Wamhoff, E.C., Blainey, P.C., et al. (2019). Multiplexed and high-throughput neuronal fluorescence imaging with diffusible probes. Nat. Commun. *10*, 4377.
17. Auer, A., Strauss, M.T., Schlichthaerle, T., and Jungmann, R. (2017). Fast, Background-Free DNA-PAINT Imaging Using FRET-Based Probes. Nano Lett. *17*, 6428–6434.
18. Chung, K.K.H., Zhang, Z., Kidd, P., Zhang, Y., Williams, N.D., Rollins, B., Yang, Y., Lin, C., Baddeley, D., and Bewersdorf, J. (2022). Fluorogenic DNA-PAINT for faster, low-background super-resolution imaging. Nat. Methods *19*, 554–559.
19. Schueder, F., Stein, J., Stehr, F., Auer, A., Sperl, B., Strauss, M.T., Schwille, P., and Jungmann, R. (2019). An order of magnitude faster DNA-PAINT imaging by optimized sequence design and buffer conditions. Nat. Methods *16*, 1101–1104.
20. Strauss, S., and Jungmann, R. (2020). Up to 100-fold speed-up and multiplexing in optimized DNA-PAINT. Nat. Methods *17*, 789–791.
21. Yurke, B., Turberfield, A.J., Mills, A.P., Jr., Simmel, F.C., and Neumann, J.L. (2000). A DNA-fuelled molecular machine made of DNA. Nature *406*, 605–608.
22. Sograte-Idrissi, S., Schlichthaerle, T., Duque-Afonso, C.J., Alevra, M., Strauss, S., Moser, T., Jungmann, R., Rizzoli, S.O., and Opazo, F. (2020). Circumvention of common labelling artefacts using secondary nanobodies. Nanoscale *12*, 10226–10239.
23. Klevanski, M., Herrmannsdoerfer, F., Sass, S., Venkataramani, V., Heilemann, M., and Kuner, T. (2020). Automated highly multiplexed super-resolution imaging of protein nano-architecture in cells and tissues. Nat. Commun. *11*, 1552.
24. Civitci, F., Shangguan, J., Zheng, T., Tao, K., Rames, M., Kenison, J., Zhang, Y., Wu, L., Phelps, C., Esener, S., and Nan, X. (2020). Fast and multiplexed superresolution imaging with DNA-PAINT-ERS. Nat. Commun. *11*, 4339.
25. Strauss, M.T., Schueder, F., Haas, D., Nickels, P.C., and Jungmann, R. (2018). Quantifying absolute addressability in DNA origami with molecular resolution. Nat. Commun. *9*, 1600.
26. Dai, M., Jungmann, R., and Yin, P. (2016). Optical imaging of individual biomolecules in densely packed clusters. Nat. Nanotechnol. *11*, 798–807.
27. Thevathasan, J.V., Kahnwald, M., Cieśliński, K., Hoess, P., Peneti, S.K., Reitberger, M., Heid, D., Kasuba, K.C., Hoerner, S.J., Li, Y., et al. (2019). Nuclear pores as versatile reference standards for quantitative superresolution microscopy. Nat. Methods *16*, 1045–1053.
28. Schlichthaerle, T., Strauss, M.T., Schueder, F., Auer, A., Nijmeijer, B., Kueblbeck, M., Jimenez Sabinina, V., Thevathasan, J.V., Ries, J., Ellenberg, J., and Jungmann, R. (2019). Direct Visualization of Single Nuclear Pore Complex Proteins Using Genetically-Encoded Probes for DNA-PAINT. Angew. Chem. Int. Ed. Engl. *58*, 13004–13008.
29. Endesfelder, U., Malkusch, S., Fricke, F., and Heilemann, M. (2014). A simple method to estimate the average localization precision of a single-molecule localization microscopy experiment. Histochem. Cell Biol. *141*, 629–638.
30. Xu, K., Zhong, G., and Zhuang, X. (2013). Actin, spectrin, and associated proteins form a periodic cytoskeletal structure in axons. Science *339*, 452–456.
31. Hisanaga, S., and Hirokawa, N. (1988). Structure of the peripheral domains of neurofilaments revealed by low angle rotary shadowing. J. Mol. Biol. *202*, 297–305.
32. Tang, A.-H., Chen, H., Li, T.P., Metzbower, S.R., MacGillavry, H.D., and Blanpied, T.A. (2016). A trans-synaptic nanocolumn aligns neurotransmitter release to receptors. Nature *536*, 210–214.
33. McInnes, L., Healy, J., and Melville, J. (2018). UMAP: Uniform Manifold Approximation and Projection for Dimension Reduction. Preprint at arXiv.. https://doi.org/10.48550/arXiv.1802.03426.
34. Karimzadeh, M., Ernst, C., Kundaje, A., and Hoffman, M.M. (2018). Umap and Bismap: quantifying genome and methylome mappability. Nucleic Acids Res. *46*, e120.
35. Becht, E., McInnes, L., Healy, J., Dutertre, C.A., Kwok, I.W.H., Ng, L.G., Ginhoux, F., and Newell, E.W. (2018). Dimensionality reduction for visualizing single-cell data using UMAP. Nat. Biotechnol. *37*, 38–44. https://doi.org/10.1038/nbt.4314.
36. Dorrity, M.W., Saunders, L.M., Queitsch, C., Fields, S., and Trapnell, C. (2020). Dimensionality reduction by UMAP to visualize physical and genetic interactions. Nat. Commun. *11*, 1537.
37. Rousseeuw, P.J. (1987). Silhouettes: A graphical aid to the interpretation and validation of cluster analysis. J. Comput. Appl. Math. *20*, 53–65.
38. Nainggolan, R., Perangin-angin, R., Simarmata, E., and Tarigan, A.F. (2019). Improved the performance of the K-means cluster using the Sum of Squared Error (SSE) optimized by using the elbow method. J. Phys, Conf. Ser. *1361*, 012015.
39. Wiesner, T., Bilodeau, A., Bernatchez, R., Deschênes, A., Raulier, B., De Koninck, P., and Lavoie-Cardinal, F. (2020). Activity-Dependent Remodeling of Synaptic Protein Organization Revealed by High Throughput Analysis of STED Nanoscopy Images. Front. Neural Circuits *14*, 57.
40. Dani, A., Huang, B., Bergan, J., Dulac, C., and Zhuang, X. (2010). Super-resolution imaging of chemical synapses in the brain. Neuron *68*, 843–856.
41. Orlando, M., Lignani, G., Maragliano, L., Fassio, A., Onofri, F., Baldelli, P., Giovedí, S., and Benfenati, F. (2014). Functional role of ATP binding to synapsin I in synaptic vesicle trafficking and release dynamics. J. Neurosci. *34*, 14752–14768.
42. Taguchi, K., Watanabe, Y., Tsujimura, A., Tatebe, H., Miyata, S., Tokuda, T., Mizuno, T., and Tanaka, M. (2014). Differential expression of alpha-synuclein in hippocampal neurons. PLoS One *9*, e89327.
43. Bartholome, O., Van den Ackerveken, P., Sánchez Gil, J., de la Brassinne Bonardeaux, O., Leprince, P., Franzen, R., and Rogister, B. (2017). Puzzling Out Synaptic Vesicle 2 Family Members Functions. Front. Mol. Neurosci. *10*, 148.
44. Bajjalieh, S.M., Frantz, G.D., Weimann, J.M., McConnell, S.K., and Scheller, R.H. (1994). Differential expression of synaptic vesicle protein 2 (SV2) isoforms. J. Neurosci. *14*, 5223–5235.
45. Dotti, C.G., Sullivan, C.A., and Banker, G.A. (1988). The establishment of polarity by hippocampal neurons in culture. J. Neurosci. *8*, 1454–1468.
46. Kaech, S., and Banker, G. (2006). Culturing hippocampal neurons. Nat. Protoc. *1*, 2406–2415.
47. Helm, M.S., Dankovich, T.M., Mandad, S., Rammner, B., Jähne, S., Salimi, V., Koerbs, C., Leibrandt, R., Urlaub, H., Schikorski, T., and Rizzoli, S.O. (2021). A large-scale nanoscopy and biochemistry analysis of postsynaptic dendritic spines. Nat. Neurosci. *24*, 1151–1162.

48. Truckenbrodt, S., Viplav, A., Jähne, S., Vogts, A., Denker, A., Wildhagen, H., Fornasiero, E.F., and Rizzoli, S.O. (2018). Newly produced synaptic vesicle proteins are preferentially used in synaptic transmission. EMBO J. *37*, e98044.

49. Xu, Q., Schlabach, M.R., Hannon, G.J., and Elledge, S.J. (2009). Design of 240,000 orthogonal 25mer DNA barcode probes. Proc. Natl. Acad. Sci. USA *106*, 2289–2294.

50. Edelstein, A.D., Tsuchida, M.A., Amodaj, N., Pinkard, H., Vale, R.D., and Stuurman, N. (2014). Advanced methods of microscope control using μManager software. J. Biol. Methods *1*, e10.

51. Schindelin, J., Arganda-Carreras, I., Frise, E., Kaynig, V., Longair, M., Pietzsch, T., Preibisch, S., Rueden, C., Saalfeld, S., Schmid, B., et al. (2012). Fiji: an open-source platform for biological-image analysis. Nat. Methods *9*, 676–682.

52. Ramdas, A., Trillos, N., and Cuturi, M. (2017). On Wasserstein two-sample testing and related families of nonparametric tests. Entropy *19*, 47.

53. Majtey, A.P., Borras, A., Casas, M., Lamberti, P.W., and Plastino, A. (2008). Jensen–Shannon divergence as a measure of the degree of entanglement. Int. J. Quantum Inform. *06*, 715–720.

54. Ester, M., Kriegel, H.-P., Sander, J., and Xu, X. (1996). A density-based algorithm for discovering clusters in large spatial databases with noise. In kdd, *96*, pp. 226–231.

55. Gardiner, J.D., Behnsen, J., and Brassey, C.A. (2018). Alpha shapes: determining 3D shape complexity across morphologically diverse structures. BMC Evol. Biol. *18*, 184.

56. McInnes, L., Healy, J., Saul, N., and Großberger, L. (2018). UMAP: Uniform Manifold Approximation and Projection. J. Open Source Softw. *3*, 861.

57. Jin, X., and Han, J. (2011). K-Means Clustering. Encyclopedia of Machine Learning. Springer US. 563–564.

58. Müllner, D. (2011). Modern hierarchical, agglomerative clustering algorithms. Preprint at arXiv. https://doi.org/10.48550/ARXIV.1109.2378.

59. Mann, H.B., and Whitney, D.R. (1947). On a Test of Whether one of Two Random Variables is Stochastically Larger than the Other. Ann. Math. Statist. *18*, 50–60.

60. Bender, R., and Lange, S. (2001). Adjusting for multiple testing–when and how? J. Clin. Epidemiol. *54*, 343–349.

61. Ferreira, J.A., and Zwinderman, A.H. (2006). On the Benjamini–Hochberg method. Ann. Stat. *34*, 1827–1849.

STAR★METHODS

KEY RESOURCES TABLE

REAGENT or RESOURCE	SOURCE	IDENTIFIER
Antibodies		
All affinity reagents used for SUM-PAINT experiments are listed with detailed information in Table S2	This study	See Table S2
sdAB anti-GFP	Nanotag	Cat#N0305;RRID:AB_3075907
Biological samples		
rat primary hippocampal neurons (Wistar albino (Rattus Norvegicus))	University medical center goettingen	RGD_13508588
Mouse brain tissue (C57BL/6J (Mus musculus))	University medical center goettingen	IMSR_JAX:000664
Chemicals, peptides, and recombinant proteins		
Magnesium chloride (1M)	Thermo Fisher Scientific	Cat#AM950G
Sodium chloride (5M)	Thermo Fisher Scientific	Cat#AM9759
Ultrapure water	Thermo Fisher Scientific	Cat#10977-035
EDTA (0.5 M, pH 8.0)	Thermo Fisher Scientific	Cat#AM9260G
1x PBS pH 7.2	Thermo Fisher Scientific	Cat#20012-019
10x PBS	Thermo Fisher Scientific	Cat#70011051
Salmon Sperm DNA	Thermo Fisher Scientific	Cat#15632011
Triton X-100	Carl Roth	Cat#6683.1
Paraformaldehyde	Electron Microscopy Sciences	Cat#15710
BSA	Sigma-Aldrich	Cat#A4503-10G
Tween 20	Sigma-Aldrich	Cat#P9416-50ML
Methanol	Sigma-Aldrich	Cat#32213-2.5L
(±)-6-hydroxy-2,5,7,8-tetra-methylchromane-2-carboxylic acid (Trolox)	Sigma-Aldrich	Cat#238813-5G
Sticky-slide 8 well chambers	Ibidi	Cat#80808
McCoy's 5A media	Thermo Fisher Scientific	Cat#16600082
glass-bottomed eight-well μ-slides	Ibidi	Cat#80827
No 1 glass slides	Marienfeld	Cat#10756991
FBS	Thermo Fisher Scientific	Cat#10500-064
90 nm gold nanoparticles	Cytodiagnostics	Cat#G-90-100
Sodium hydroxide	VWR	Cat#31627.290
protocatechuate 3,4-dioxygenase pseudomonas (PCD)	Sigma-Aldrich	Cat#P8279
3,4-dihydroxybenzoic acid (PCA)	Sigma-Aldrich	Cat#37580-25G-F
Neutravidin	Thermo Fisher Scientific	Cat#3100
Biotin-labeled BSA	Sigma-Aldrich	Cat#A8549
0.05% trypsin-EDTA	Thermo Fisher Scientific	Cat#25300-054
Tris (1M)	Thermo Fisher Scientific	Cat#AM9855G
Dextran sulfate 50% solution	VWR	Cat#E516-100ML
Ethylencarbonate	Sigma-Aldrich	Cat#E26258
20xSSC	Thermo Fisher Scientific	Cat#AM9763
bifunctional maleimide-DBCO linker	Sigma-Aldrich	Cat#760668
Sodium hydroxide	VWR	Cat#31627.290
Ammoniumchloride	Merck	Cat#12125-02-9

(*Continued on next page*)

Continued		
REAGENT or RESOURCE	SOURCE	IDENTIFIER
Deposited data		
All experimental data is deposited at Zenodo	This study	https://doi.org/10.5281/zenodo.10212680
Experimental models: Cell lines		
U2OS-CRISPR-Nup96-mEGFP	Ellenberg/Ries lab EMBL Heidelberg	N/A
Oligonucleotides		
Secondary Label Oligos	Metabion	see Table S1
Primary Barcode Oligos	Metabion	see Table S1
DNA origami staples	Integrated DNA Technologies	see Table S1
Software and algorithms		
Custom analysis software	This study	https://doi.org/10.5281/zenodo.10212680
Picasso	Schnitzbauer et al., 2017[13]	https://github.com/jungmannlab/picasso

RESOURCE AVAILABILITY

Lead contact

Further information and requests for resources and reagents should be directed to and will be fulfilled by the lead contact, Ralf Jungmann (jungmann@biochem.mpg.de).

Materials availability

This study did not generate new unique reagents.

Data and code availability

- Raw localization microscopy datasets (in hdf5 format) and movie files for rotated synapses have been deposited at Zenodo and are publicly available as of the date of publication. The DOI is listed in the key resource table.
- All original code has been deposited at Zenodo and is publicly available as of the date of publication. DOIs are listed in the key resource table.
- Any additional information required to reanalyze the data reported in this paper is available from the lead contact upon request.

EXPERIMENTAL MODEL AND STUDY PARTICIPANT DETAILS

Animals

Wild-type Wistar rat pregnant mothers or pups (*Rattus norvegicus*), E18 (embrios) or P2 (postnatal), mixed sex cultures and adult mice (*Mus musculus*), 5 months old males and females, were obtained from the University Medical Center Göttingen and were handled according to the specifications of the University of Göttingen and of the local authority, the State of Lower Saxony (Landesamt für Verbraucherschutz, LAVES, Braunschweig, Germany). Animal experiments were approved by the local authority, the Lower Saxony State Office for Consumer Protection and Food Safety (Niedersächsisches Landesamt für Verbraucherschutz und Lebensmittelsicherheit). Animals were not used in other studies, maintained on a standard chow diet, kept at room temperature under a constant light cycle, and screened regularly for common rodent viruses and pathogens. Embryos were obtained from pregnant female rats not used in other studies. P2 animals were left with the female prior to sacrifice. Animals of both sexes were used in this study, as cultures were prepared from male and female rat embryos in a 1:1 ratio, and mouse brain slices were obtained from both male and female mice.

Primary cell culture

Primary hippocampal neuron cultures from embryonic day 18 (E18) Wistar rat embryos were prepared with minor adaptations from a previous work.[47] Briefly, upon dissection neurons were grown on 1 mg/mL poly-L-lysine coated coverslips over an astrocyte feeder layer and were kept in an N2-supplemented serum-free medium.[46] To prepare for the dissection of E18 rats, glial cells were prepared from P2 Wistar rat pups and seeded in 12-well plates at a density of 10000 cells per well, three days prior. Next, hippocampal neurons were seeded onto 18 mmØ coverslips at a density of 60000 cells per coverslip, with paraffin dots acting as a spacer between the neurons and glial cells. 500 μL of the cell culture medium was exchanged with fresh medium twice a week. Following this culture

method, the neurons developed proper polarity, generated intricate axonal and dendritic networks, and established multiple functional synaptic connections with each other.[46] Mixed glial and neuronal cultures were prepared from P2 rats, as previously described.[48]

Cell lines

U2OS-CRISPR-Nup96-mEGFP cells (a gift from the Ries and Ellenberg laboratories) were cultured in McCoy's 5A medium (Thermo Fisher Scientific, 16600082) supplemented with 10% FBS. For super-resolution imaging 50k cells were seeded 24 h before fixation in glass-bottomed eight-well μ-slides (ibidi, 80827).

METHOD DETAILS

Buffers

The following buffers were used for sample preparation and imaging

(1) Buffer C+: 1× PBS, 500 mM NaCl and 0.05% Tween 20
(2) Buffer C: 1× PBS, 500 mM NaCl
(3) Antibody Incubation buffer: 1×PBS, 1 mM EDTA, 0.02% Tween 20, 0.05% NaN_3, 2% BSA and 0.05 mg/mL sheared salmon sperm DNA
(4) Blocking Buffer: 1x PBS, 3% BSA, 0.25%Triton X-100 and 0.05 mg/mL sheared salmon sperm DNA
(5) Buffer A+: 10 mM Tris pH 8, 100 mM NaCl and 0.05% Tween 20
(6) Buffer B+: 10 mM MgCl2, 5 mM Tris-HCl pH 8, 1 mM EDTA and 0.05% Tween 20, pH 8
(7) Buffer B: 10 mM MgCl2, 5 mM Tris-HCl pH 8 and 1 mM EDTA, pH 8
(8) Optimized hybridization buffer: 10% Dextran Sulfate, 10% Ethylencarbonate, 4xSSC and 0.4% Tween 20
(9) Dehybridization buffer: 10% Dextran Sulfate, 20% Ethylencarbonate, 2xSSC

Oxygen scavenging system preparation

The following workflow describes the preparation of stock solutions for the oxygen scavenging system used to supplement the imaging buffer described in Table S3:

Trolox (100×) was made by the addition of 100 mg of Trolox to 430 μL of 100% methanol and 345 μL of 1 M NaOH in 3.2 mL of water. PCA (40×) was made by mixing 154 mg of PCA in 10 mL of water and NaOH and adjustment of pH to 9.0. PCD (100×) was made by the addition of 9.3 mg of PCD to 13.3 mL of buffer (100 mM Tris-HCl pH 8.0, 50 mM KCl, 1 mM EDTA, 50% glycerol).

Primary label design

The primary labels were shortened from 25 bases to 20 bases from the repository containing 240000 unique sequences.[49] The sequences were designed with melting temperatures between 58°C and 68°C. We first truncated the sequences to 20 bases by removing any five nucleotides randomly from the original sequence. We blasted the resulting sequences against the mouse genome to select the ones that show 14 bases or less homology to the genome. The remainder was further screened to contain 48%–65% GC-content. We then evaluated each sequence both for intramolecular and intermolecular secondary structures of seven base-pairs or longer. Sequences that showed seven or more base-pair interactions were excluded from the list As a result our stringent selection criteria yielded 240 sequences of which we selected 42 for our DNA Origami experiments. These resulting sequences were selected as primary labels, extended with DNA origami staple sequences shown in Table S1 for incorporation in rectangular DNA origami nanostructures. Secondary labels are reverse complements of the primary labels, extended with speed-optimized docking sequences[20] at one end and an eight-nucleotide extension (GGTCTTGTGG) on the other end for toehold-mediated strand displacement.

DNA origami sample preparation

Origami sample preparation was done in a 6-channel μ-slide (Ibidi Cat.: 80607). First 50 μL of biotin labeled bovine albumin (1 mg/mL, dissolved in buffer A+) was flushed into the chamber and incubated for 3 min. The chamber was subsequently washed with 1 mL of buffer A+ followed by incubation with 200 μL of neutravidin (0.5 mg/mL, dissolved in buffer A+) for 3 min. Afterward the chamber was washed again with 1 mL of A+ and 1 mL of B+ buffer and incubated with biotin-labeled DNA origami (~200 p.m. in buffer B+) for 3 min. Subsequently, the sample was washed with 1 mL B+ buffer and 1 mL 2xSSC buffer. Secondary label incubation was performed at a concentration of 100 nM for 15 min in optimized hybridization buffer. Finally, the chamber was washed with 5 mL of 2xSSC buffer and 1 mL of B+ buffer and 1 mL of imager solution (see Table S3) was applied for imaging.

U2OS Nup96-EGFP cell sample preparation

U2OS-Nup96-mEGFP cells were fixed with 4% paraformaldehyde for 20 min at room temperature. After fixation, the cells were washed three times with PBS before they were quenched using 0.1 M NH_4Cl in PBS for 5 min. Permeabilization and blocking was

performed simultaneously in Blocking buffer (3% BSA, 0.25% Triton X-100) for 45 min. Gold nanoparticles were incubated for 5 min as fiducial markers, followed by three times washing with PBS. Specific labeling of the mEGFP was done with anti-GFP nanobodies at an approximate concentration of 50 nM in Antibody incubation buffer at 4°C overnight. The next day, the sample was washed four times with PBS and once with buffer C and 2xSSC Buffer. Secondary label incubation was performed in the optimized hybridization buffer at a concentration of 100 nM for 20 min. Afterward, the sample was washed five times with 2xSSC buffer, once with buffer C and once with imaging solution according to Table S3.

Nanobody-DNA conjugation via single cysteine

Nanobodies against GFP (cat: N0305), tagFP (cat: N0501), rabbit and mouse IgG (cat: N2405 & N2005) were purchased from NanoTag Biotechnologies with a single ectopic cysteine at the C-terminus for site-specific and quantitative conjugation. The conjugation to DNA-PAINT docking sites (see Table S1) was performed as described previously.[22] First, buffer was exchanged to 1× PBS +5 mM EDTA, pH 7.0 using Amicon centrifugal filters (10k MWCO) and free cysteines were reacted with 20-fold molar excess of bifunctional maleimide-DBCO linker (Sigma Aldrich, cat: 760668) for 2–3 h on ice. Unreacted linker was removed by buffer exchange to PBS using Amicon centrifugal filters. Azide-functionalized DNA was added with 3–5 M excess to the DBCO-nanobody and reacted overnight at 4°C. Unconjugated nanobody and free azide-DNA was removed by anion exchange using an ÄKTA Pure liquid chromatography system equipped with a Resource Q 1 mL column. Nanobody-DNA concentration was adjusted to 5 μM (in 1xPBS, 50% glycerol, 0.05% NaN3) and stored at −20°C.

Antibody performance metric

Antibodies for SUM-PAINT experiments were screened the following way: First the primary antibodies in question (mostly knockout validated) were evaluated for specific binding according to manufacturer's examples and prior studies with confocal and STED imaging using dye coupled secondary nanobodies. After this first performance test, the antibodies were further evaluated with singleplex DNA-PAINT imaging using a secondary nanobody coupled to a docking strand. If the antibody showed similar performance in both STED and DNA-PAINT, it was assembled into a multiplexing pipeline and evaluated with 12 plex SUM-PAINT imaging. Only antibodies yielding similar performance among all the steps were then taken for the final SUM-PAINT measurements and considered "well performing" (Table S2).

SUM-PAINT imaging

SUM-PAINT DNA origami sample preparation

Origami sample preparation was done as for the secondary label origami case with the exception of DNA origami concentration being 100 p.m. per DNA origami, resulting in a total of 4.2 nM for all 42 different DNA origami. Secondary label incubation for barcoding was performed with 100 nM per secondary label (Table S1), a total of 600 nM for six strands. Imager solution was applied with concentrations according to Table S3 with five times washing with buffer B in-between readout rounds. After barcoding round one, the sample was washed once with buffer B and twice with 2xSSC buffer. 100 nM per toehold strand (Table S1), a total of 600 nM, was applied in Dehybridization buffer and incubated for 15 min. Finally, the chamber was washed five times with 2xSSC buffer and once with buffer B before proceeding to the next barcoding round (Table S3).

Neuron imaging

Rat primary hippocampal neurons were fixed using 4% paraformaldehyde for 30 min at room temperature, washed four times with PBS. After fixation, neurons were quenched using 100 mM NH_4Cl (Merck, 12125-02-9) in PBS. Then, samples were washed three times with PBS and incubated in Blocking buffer for blocking and permeabilization for 45 min. Afterward, the samples were washed with PBS, and gold nanoparticles (1:3 dilution in PBS) were incubated for 5 min and subsequently used as fiducial markers. Primary label hybridization was performed following the order described in Table S3, starting with a preincubation of the antibody with their respective secondary nanobody (NanoTag Biotechnologies GmbH) in 10 μL of antibody incubation buffer at room temperature for 2 h. After preincubation, an excess (molar ratio of 1:2) of unlabeled secondary nanobody was introduced for 5 min (NanoTag Biotechnologies, cat: K0102-50). Subsequently, a subset of six independently preincubated primary antibody and secondary nanobody complexes were pooled in 300 μL antibody incubation buffer and added to the fixed neuron sample for 60 min. Then, the sample was washed five times with PBS and once with buffer C, followed by a postfixation with 2.4% paraformaldehyde for 7 min. Afterward, the sample was quenched with 100 mM NH_4Cl in PBS and finally rinsed with 2xSSC buffer. The secondary label hybridization for barcoding round 1 was then carried out according to Table S3 with 100 nM of each secondary label for 15 min. Finally, the sample was washed five times with 2xSSC buffer and once with buffer C and imaging buffer was applied according to Table S3. After the imaging, the sample was washed three times with 2xSSC and 600 nM (100 nM per strand) blocking strands (Table S1) were applied to the sample for 15 min for signal extinction (optionally supplemented with 600 nM Toehold-strands). The next barcoding round containing six targets was carried out identically, with the pooling of the preformed primary antibodies and nanobody complexes (see Table S3 for barcoding rounds of all experiments). As a last target, Actin was imaged with the imager concentration reported in Table S3. Note that for the 12-plex demonstration (Figure S2) primary antibody incubation was done in two subsequent steps of six primary antibodies + their respective secondary nanobodies prior to imaging.

Microscope setup

Imaging was carried out using an inverted microscope (Nikon Instruments, Eclipse Ti2) equipped with a Perfect Focus System using the objective-type TIRF configuration with an oil-immersion objective (Nikon Instruments, Apo SR TIRF 100X, NA 1.49, oil). A 561 nm laser (MPB Communications, 1 W) was used for excitation and was coupled into a single-mode fiber. The laser beam was passed through a cleanup filter (Chroma Technology, ZET561/10) and coupled into the microscope objective using a beam splitter (Chroma Technology, ZT561rdc). Fluorescence light was spectrally filtered with an emission filter (Chroma Technology, ET600/50m) and imaged with an sCMOS camera (Andor, Zyla 4.2 plus) without further magnification, resulting in an effective pixel size of 130 nm after 2 × 2 binning, leading to a imaging field of view of approximately 66x66 μm^2. The camera readout sensitivity was set to 16-bit and the readout bandwidth to 200 MHz. Image acquisition and microscope control was performed using μManager.[50] For detailed imaging parameters see Table S3.

Super-resolution reconstruction

Raw DNA-PAINT data was reconstructed to super-resolution images with the Picasso software package (latest version available at https://github.com/jungmannlab/picasso). Drift correction was performed with a redundant cross-correlation following gold particles as fiducials for cellular experiments. Alignment of Exchange-PAINT and SUM-PAINT subsequent imaging rounds was performed using gold particles.

STED imaging

Immunostaining of mixed synapses in primary hippocampal neurons from E18 and P2 cultures

For the time series experiment, neurons were fixed at 8, 12, 17 and 21 days *in vitro* (DIV). For the neurotransmitter receptor experiment, 22 DIV neurons were incubated live in conditioned media containing either guinea pig anti-$GABA_A$ receptor γ2 subunit (1:100 dilution, Synaptic Systems, 224004) or mouse anti-GluA primary antibodies (1:100 dilution, Synaptic Systems, 182411C3, premixed with FluoTag-X2 anti-Mouse IgG conjugated to STAR580, NanoTag Biotechnologies, N1202-Ab580) for 30 min at 37°C. After incubation, neurons were quickly washed in cold Tyrode's buffer (124 mM NaCl, 2.7 mM KCl, 10 mM Na_2HPO_4, 2 mM KH_2PO_4, pH 7.3) and fixed as described above. After fixation and quenching with 100 mM NH_4Cl in PBS, neurons were incubated for 15 min at room temperature (RT) in a blocking buffer containing 2% bovine serum albumin (AppliChem, A1391,0500) and 0.1% Triton X-100 (Sigma Aldrich, 9036-19-5, X100-500mL) in PBS. The following steps were performed at RT. After, neurons were incubated in the same blocking buffer containing mouse anti-Gephyrin antibodies (1:200 dilution, Synaptic Systems 147011) for 1 h. Then neurons were washed three times in PBS for 5 min. After primary antibody incubation, neurons were stained in blocking buffer containing secondary anti-mouse STAR635P antibodies (1:200 dilution, in-house conjugated mouse antibodies Jackson ImmunoResearch 715-005-151 and STAR635P NHS ester Abberior 07679), anti-VGlut1 primary nanobodies conjugated to STAR580 (1:500 dilution, NanoTag Biotechnologies, N1602-Ab580-L) and anti-guinea pig AF488 antibodies (1:200 dilution, in-house conjugated guinea pig antibodies Jackson ImmunoResearch 706-005-148 and Alexa Fluor 488 NHS Ester, Molecular Probes 10266262) for 1 h. Finally, neurons were washed three times in PBS for 5 min and mounted.

Tissue sections and immunostaining of mixed synapses in the mouse brain

To image mixed synapses in adult mouse brain tissue, mice underwent perfusion with PBS followed by 4% paraformaldehyde (PFA) in PBS. After 5 min of PFA perfusion, the brain was removed and further fixed overnight in 4% PFA. Coronal sections were obtained by sectioning the brain at 30 μm thickness using a vibrating microtome (VT1200S, Leica Biosystems) and stored at 4°C in PBS supplemented with 0.02% NaN_3. For immunostaining, brain sections were first washed with PBS and quenched in 100 mM glycine (Merck, 56406) in PBS for 15 min. Sections were blocked in a blocking solution containing 10% Normal Donkey Serum (LIN-END9000-500, Histoprime Linaris), 1% BSA, 0.6% Triton X-100 in PBS for 2 h. Mouse anti-Gephyrin primary antibodies were premixed at a 1 : 2.5 M ratio with in-house produced anti-Mouse Ig kappa light chain nanobodies conjugated to STAR635P (ST635P-0003-1MG, Abberior) in 10μL for 15 min. Then, the premixture was diluted to 300 μL with blocking solution supplemented with anti-VGlut1 primary nanobodies conjugated to STAR580 (1:250 dilution, NanoTag Biotechnologies, N1602-Ab580-L) and tissue sections were stained with this solution overnight at 4°C. On the following day tissue sections were washed with blocking solution 3 times for 10 min, followed by 2 washes with high-salt PBS (PBS with 500 mM NaCl, Merck, 7647-14-5), incubated with Höchst33342 (1:10000 dilution, Thermofisher Scientific, 62249) and washed 2 times with PBS for 10 min. After these washes tissue sections were mounted.

Synaptotagmin 1 lumenal (Syt1-lum) antibody uptake assay

18 DIV primary hippocampal neurons were incubated live in their media containing rabbit anti-Synaptotagmin 1 antibodies directly conjugated to STAR635P targeting the lumenal side of Syt1 (1:150 dilution, Synaptic Systems 105 308Ab635P) for 30 min at 37°C to allow synaptic vesicle recycling which occurs spontaneously due to network activity in our cultures.[48] After incubation, neurons were quickly washed in cold Tyrode's buffer, fixed and quenched as described above. After short washes in PBS, neurons were blocked and permeabilized in 10% Normal Donkey Serum and 0.3% Triton X-100 in PBS for 15 min. Following this step, neurons were incubated in the blocking and permeabilization buffer containing mouse anti-Gephyrin antibodies (1:200 dilution, Synaptic Systems 147011) for 1 h at RT. Excess of primary antibodies was washed with PBS supplemented with 0.05% Tween 20 (Tween 20, Merck 9005-64-5) three times for 5 min. After washes, neurons were incubated in the blocking and permeabilization buffer containing donkey anti-mouse AF488 secondary antibodies (1:200 dilution, in-house conjugated mouse antibodies Jackson ImmunoResearch 715-005-151 and Alexa Fluor 488 NHS Ester, Molecular Probes 10266262) and anti-VGlut1 primary nanobodies

conjugated to AzDye568 (1:500 dilution, NanoTag Biotechnologies, N1602-AF568-L) for 1 h. Following this incubation, neurons were washed in PBS with 0.05% Tween 20 three times for 5 min and mounted.

STED sample mounting

The coverslips were quickly dipped in ddH_2O to remove excess salts, the side of the coverslip was quickly dried on a kimwipe tissue to remove excess liquid. Immediately after, the coverslips were mounted on a microscope slide using 10 μL of Prolong Glass Antifade mounting media (ThermoFisher, P36980), left to harden overnight at RT. In the case of tissue sections, following the stainings the tissue was placed on a coverslip, the excess of PBS was cleaned with a kimwipe and mounted using Prolong Glass Antifade mounting media (ThermoFisher, P36980), which was left to harden overnight at RT. All samples were stored at 4°C until they were imaged in the following days.

STED image acquisition of mixed synapses

STED images were acquired using an Abberior microscope setup (Abberior Instruments GmbH) featuring an Olympus IX83 microscope body and operated with the Imspector software (version 16.3.14287-w2129 and 16.3.15521-w2209). Hippocampal CA1 *stratum radiatum* region in mouse brain tissue sections was identified by nuclear staining. Samples were imaged using a UPLSAPO100× O objective (1.4 NA), single z-plane images with a size of 20 × 20 μm^2 (20 × 20 nm^2 pixel size) were collected for each coverslip or a size of 60 × 60 μm^2 (40 × 40 nm^2 pixel size) were collected for tissue section overview. Custom size images (with a 20 × 20 nm pixel size) were collected in the tissue section overview region, where a mixed synapse was identified. AF488 fluorophores were excited with 485 nm laser, depleted with 595 nm pulsed laser, and the emission was detected in the range of 500–550 nm in STED mode. STAR580 and STAR635P fluorophores were excited with 561 nm and 640 nm pulsed lasers, respectively, depleted with 775 nm pulsed laser, and the emission was detected in the range of 605–625 nm and 650–720 nm, respectively, in STED mode.

STED image analysis of mixed synapses

Image analysis was performed using in-house written ImageJ/Fiji[51] macro. Briefly, binary masks of VGlut1, Gephyrin and Syt1-lum positive regions were obtained by applying a 1 sigma radius Gaussian blur filter and setting a user-defined threshold. Such objects were filtered by area (0.05–0.8 μm^2 for VGlut1, 0.02–0.4 μm^2 for Gephyrin and 0.03–2 μm^2 for Syt1-lum) and counted for every image. An overlap between VGlut1 and Gephyrin was manually identified by selecting a fixed size circle ROI around the overlap. Such regions were defined as "$VGlut1^+$–$Gephyrin^+$", counted and expressed as percentage over the total number of synaptic clusters (sum of VGlut1 and Gephyrin regions). For Syt1-lum analysis, Syt1-lum intensity was measured in the presynapse of excitatory ($VGlut1^+$-$Gephyrin^-$), inhibitory ($VGlut1^-$-$Gephyrin^+$) and mixed ($VGlut1^+$-$Gephyrin^+$) synapses and expressed as Syt1 fluorescence intensity normalized by the area.

QUANTIFICATION AND STATISTICAL ANALYSIS

DNA origami binding kinetics and hybridization and displacement efficiency

For binding kinetics and hybridization and displacement efficiency calculation, DNA origami were handpicked using a radius of 1.2 pixels (156 nm). For the binding kinetics analysis, 400 origami were picked per dataset, for the hybridization and displacement calculation as a function of time 250 origami were picked and for the 42-plex hybridization and displacement efficiency 6440 origami were picked. Binding kinetics were then calculated on individual DNA origami sites by extracting the mean bright and dark time of all individual sites with a radius of 0.08 pixel (10.4 nm) with the picasso analysis package. Efficiency calculation was performed with single-molecule clustering, identifying the number of individual binding sites for each origami. Min sample size and cluster radius were calculated based on the localization precision of the measurement and average numbers of localizations for individual binding sites (hybridization analysis: 6 nm, 25 localizations, displacement analysis: 6 nm, 45 localization, 42-plex 5 nm, 15 localizations).

Synapse segmentation

Synapse segmentation was interactively performed using the Picasso[13] pick tool with a circular selection region of 800 nm diameter. An alignment of presynaptic and postsynaptic proteins Bassoon, Homer1 and Gephyrin displaying a clearly identifiable synaptic cleft were used as selection criteria for the first round. In a second round, the regions were selected again based on the presence of neurotransmitter transporter proteins VGlut1 and VGAT combined with common vesicle pool proteins Synaptotagmin1 and Synapsin. The selection yielded 890 synaptic regions.

Dataset preparation for the analysis

In this study, six datasets were analyzed. Datasets included different numbers of proteins and synapse picks, where we have Dataset 1 (21 proteins, 144 synapse picks), Dataset 2 (19, 131), Dataset 3 (17, 154), Dataset 4 (21, 186), Dataset 5 (21, 100) and Dataset 6 (14, 173) (Figure S4B; Table S3).

Feature extraction

The feature extraction process was divided into (i) histogram feature extraction and (ii) clustering feature extraction. For histogram feature extraction, a 3D histogram of the super-resolution localizations of the proteins was calculated. For each histogram, the localizations were decentred and normalized by mapping to [-1,1].[3] Then the 3D histogram with 8000 3D bins (20 bins in each dimension) was calculated. This histogram generation allowed the calculation of, mean, standard deviation, skewness, kurtosis, entropy,

minimum, maximum and entropy (all unitless due to normalization). In addition, the pairwise Wasserstein distance,[52] Jensen Shannon distance,[53] and cosine distance of the histograms of different proteins were obtained. For clustering feature extraction, spatial clustering using DBSCAN[54] was performed for each protein species in each segmented synapse. DBSCAN parameters, minimum localizations, and clustering radius were selected based on the imaging parameters of the individual super-resolution channel of the protein. Background regions were taken as a base for determining the cluster minimum localization number and both DBSCAN parameters were further adjusted based on visual validation on selected synapses to determine a cutoff value distinguishing background from specific protein clusters. All clustering parameters for the individual datasets and protein channels can be found in Table S5. Afterward, the largest cluster based on the number of localizations for each protein was classified as the main cluster. In addition to the number of localizations, spatial cluster size, Center of Mass (CoM) and convex hull volume (unit = px^3) of each cluster were calculated. In addition, we used α-shape[55] with $\alpha = 0.5$ to calculate the cluster volume (unit = px^3) and surface area (unit = px^2). Finally, the distance between the CoM (unit = px) of each protein species was calculated (Table S4). Considering that some of the datasets did not contain all of the proteins, the features were input with 0 to enable further numerical evaluations. For the analysis of single features with pixel-based units, these features were transformed to nm-based values to provide meaningful values.

In total, 2537 features were extracted for each of the 890 synapses. This feature space contained 171 histogram-based features (HF) for a single protein channel and 1450 pairwise histogram-based features (HD), comparing features between protein targets. On the spatial clustering feature side, our extraction contained 796 clustering-based features (CF) for single-protein channels and 48 features comparing the CoM distance between protein species (CD). Finally, for the α-shape based volume and surface area, we extracted 72 features for single-protein channels (AS). To assemble a comparable feature selection between the six datasets, only proteins imaged in all six datasets were considered for the analysis Moreover, constant features (i.e., no variance) were excluded from the analysis as they provided no information, yielding to 1590 features.

Unsupervised learning with dimensionality reduction and clustering

To reduce the dimensionality of the datasets to aid data interpretation, we used Uniform Manifold Approximation and Projection (UMAP). Since we were pooling segmented synapses from different datasets, the slight variation of experimental conditions was due to minor changes in sample preparation or different imaging parameters. We hence used feature normalization to be able to compare synapses from different datasets robustly. For an extracted feature, f we calculated $f_{dataset}^{normalized} = (f_{dataset} - \mu_{dataset})/\sigma_{dataset}$ where $\mu_{dataset}$ and $\sigma_{dataset}$ are mean and standard deviation of feature f among all synapse picks per dataset. For example, when we consider the number of localizations as a single feature $f_{dataset}$, there are variations between the datasets because of different imager concentrations and positions of the cell in the imaging volume. We then calculate $f_{dataset}^{normalized}$ considering $\mu_{dataset}$ and $\sigma_{dataset,}$ of all synapses in the datasets, yielding features with mean = 0 and standard deviation = 1 for each dataset. Therefore, the features among the datasets can be comparable after the normalization.

To reduce the dataset's high dimensionality while learning the feature space's structure, uniform manifold approximation and project (UMAP) was used.[56] The reason for this choice is UMAP's robustness in dealing with high-dimensional data and its efficiency in terms of run time.[35] We used the Python implementation of umap-learn (version = 0.5.1) withdefault parameters, including n_neighbors = 15, min_dist = 0.1, n_components = 2, and metric = 'euclidean'. This reduced 1590 features to a 2-dimensional space (n_component = 2). Next, we focused on understanding the structure of the 2-dimensional space. For selecting the number of clusters, we used the Silhouette score, which measures the similarity of data points within a cluster compared to other clusters.[37] It ranges from −1 to 1, where the higher value indicates more similarity within the points in their designated clusters. In our analysis, KMeans clustering was performed for K = 2,3, …,10, and the results showed the maximum score achieved by K = 3. Additionally we also implemented the elbow method.[38] In this method, the clustering is done for k = 1,2, …,10. Then for each value of k, the sum of squared distances from each point to its assigned center (within-cluster sum of squares or WCSS). Plotting WCSS values vs. the number of clusters leads to a decreasing plot, where the optimal number of clusters is where the decrease in the WCSS begins to level off, hence the name "elbow". In our case, for k>=3, WCSS the decrease becomes less pronounced, therefore k = 3 is the optimal number of clusters. We thus applied KMeans clustering[57] with k = 3 from scikit-learn (version = 0.24.2). The resulting clusters from the UMAP, Figure 5B were then assigned as the three synaptic subtypes under investigation, namely inhibitory, mixed and excitatory synapses. To visualize the variation of a single feature (e.g., numbers of localizations of Bassoon) on an individual synapse level we rendered the UMAP with a grayscale color for each synapse ranging from minimum value (white) to maximum value (black) for the given feature.

Center of mass matrix

The CoM distance matrix was assembled based on the 48 features extracted as pairwise CoM distances for protein clusters. The single pairwise CoM between two protein species is the absolute distance between the CoM of DBSCAN-detected protein clusters in a single synapse. To assemble the matrix, only synapses that expressed a spatial cluster in both protein channels were taken into account. For the overall CoM matrix (Figure 6C), the average of all segmented synapses was taken to calculate the average CoM distance, while the synapse subtype-specific proteins Homer1, Gephyrin were pooled as a postsynaptic scaffold (PSS), and VGlut1 and VGAT were pooled as neurotransmitter transporter (NTT). For the assembly of synapse subtype-specific CoM matrices (Figure S6A), the synapse subtype-specific proteins were separated.

Relative abundance analysis and spatial cluster volume

For calculating the relative abundance of a given protein species among the three synapse subtypes, we considered the detected and not detected clusters by spatial clustering with DBSCAN. If the segmented synapse is expressing a protein cluster, which was detected by DBSCAN we label this protein species with a 1. If the cluster detection threshold is not sufficient, we assign a 0. The relative abundance is then calculated as the ratio between the number of detected spatial clusters for a given protein and the total number of synapses. As an example, since the synapse selection was based on a positive DBSCAN spatial clustering on Bassoon, all synapses express a protein cluster in this protein channel and the relative abundance for Bassoon is 100%. To further investigate the specifics of the spatial protein clusters detected by DBSCAN, we plotted the average absolute volume calculated by α-shape in a heatmap, separated for the synaptic subtypes.

Distance profile

To assemble a representative distance profile for each synaptic subtype, three synapses, one for each subtype, were selected and rotated *en-face*. We then plotted the localizations for each protein channel of the three synapses in a violin plot, with the distance between the mean of the pre- and postsynaptic scaffold proteins as 0. The polarity of the synapse was assigned such that the postsynaptic scaffold would be on the negative side and the presynaptic scaffold on the positive. Only protein channels in which the DBSCAN spatial clustering detected a relevant cluster for the selected synapse were taken for representation.

Volume ratio correlation

To make a conclusive comparison between the expression level of different proteins, we considered the volume of a given protein species, calculated by α-shape as a proxy. The volume of the protein is the only feature that can be considered for abundance comparison between protein species since the number of localizations depends heavily on the labeling efficiency of the antibody. We first separated the synapses based on their subtype, then plotted the pairwise volume ratio of each protein rendering each individual synapse and calculated the Pearson correlation for the two proteins. For example, we can consider the volume correlation between the synaptic vesicle protein Synaptotagmin1 and the NTT. Since both proteins are associated with the vesicle pool, the direct comparison between the volume ratio of those proteins yields relatively high correlation values for all three synaptic subtypes ($r = 0.82$ for excitatory, $r = 0.6$ for inhibitory, $r = 0.86$ for mixed). We assembled an 11x11 matrix showing all correlation values (grayscale 0 to 1) for an overall comparison of all pairwise protein values. To compare these matrices between the synaptic subtypes, we kept the protein order the same for each matrix, allowing a direct visual inspection of differences and similarities. Finally, to make a more quantitative comparison of the volume correlation within one synaptic subtype, we performed hierarchical clustering and assembled a dendrogram for each matrix. The hierarchical clustering was based on the nearest neighbor point algorithm and Euclidean distance[58] based on SciPy (version = 1.8.0) implementation.

Statistical tests among features and clusters

To assess if there is a significant difference between the distributions of synapse volumes and the number of localizations of individual protein species among the three synaptic subtypes in Figure 6H we systematically compared the features with Wilcoxon-Mann-Withney U Test.[59] This test is a non-parametric test with no assumption on the distribution of the data. A significant difference between distributions in this test is indicated by a p value <0.05, indicated by an asterisk (*) in the figure. To correct for multiple testing and reduce the false discovery rate,[60] all p values were corrected using the Benjamini-Hochberg procedure.[61]

CellPress
OPEN ACCESS

Supplemental figures

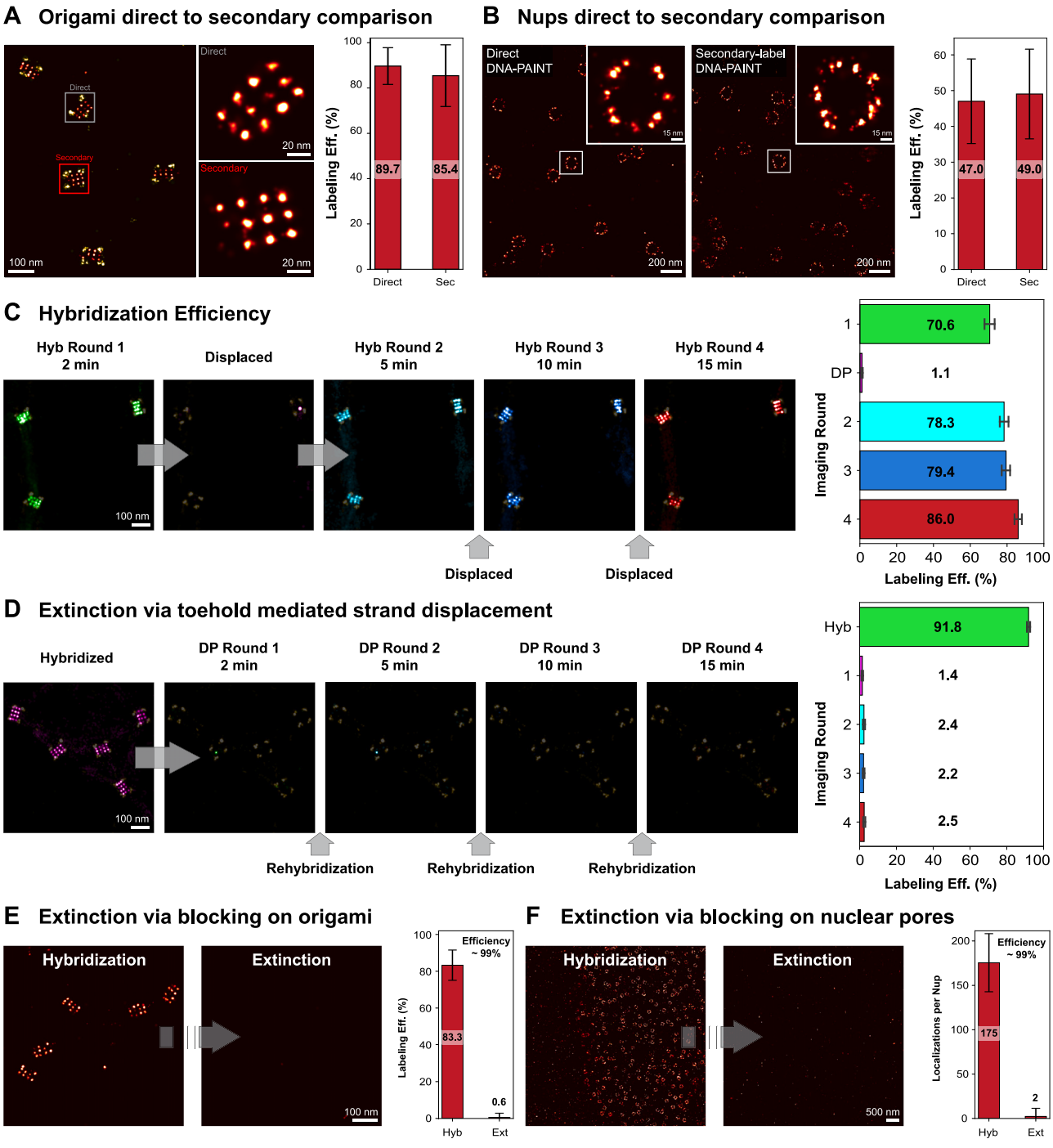

Figure S1. Secondary-label based DNA-PAINT optimization, related to Figure 2

(A) Comparison of secondary-label based DNA-PAINT to direct DNA-PAINT on DNA origami. The comparison of the labeling efficiency (calculated as detected binding sites over number of expected binding sites (x/12)) indicates no significant difference in labeling performance. (Binding sites were detected with 2D single molecule clustering).

(legend continued on next page)

(B) Comparison of secondary-label based DNA-PAINT to direct DNA-PAINT on nuclear pore complexes. The comparison of the labeling efficiency (calculated as detected binding sites over number of expected binding sites (x/32)) indicates no significant difference in labeling performance. (Binding site were detected with 3D single molecule clustering).
(C) Hybridization efficiency optimization on DNA origami. The hybridization efficiency is evaluated by a time-series featuring 2 min, 5 min, 10 min and 15 min of hybridization time, each followed by 15 min of signal extinction by toehold-mediated strand displacement. The resulting labeling efficiency (a combination of primary barcode incorporation and secondary label hybridization efficiency) of 250 origami and one exemplary experiment is shown by a bar plot.
(D) Extinction via toehold-mediated strand displacement optimization on DNA origami. The extinction efficiency is evaluated by a time-series featuring 2 min, 5 min, 10 min and 15 min of extinction time, each followed by 15 min of signal rehybridization. The resulting extinction efficiency of 250 origami and one exemplary experiment is shown by a bar plot.
(E) Extinction via blocking evaluation on DNA origami. 2 min extinction via blocking yields similar results to the toehold-mediated strand displacement with 99% efficiency (calculated by 2D single molecule clustering).
(F) Extinction via blocking evaluation on nuclear pores. 15 min extinction via blocking on nuclear pores shows a 99% extinction efficiency (calculated by localization comparison in all nuclear pores from the hybridization round).

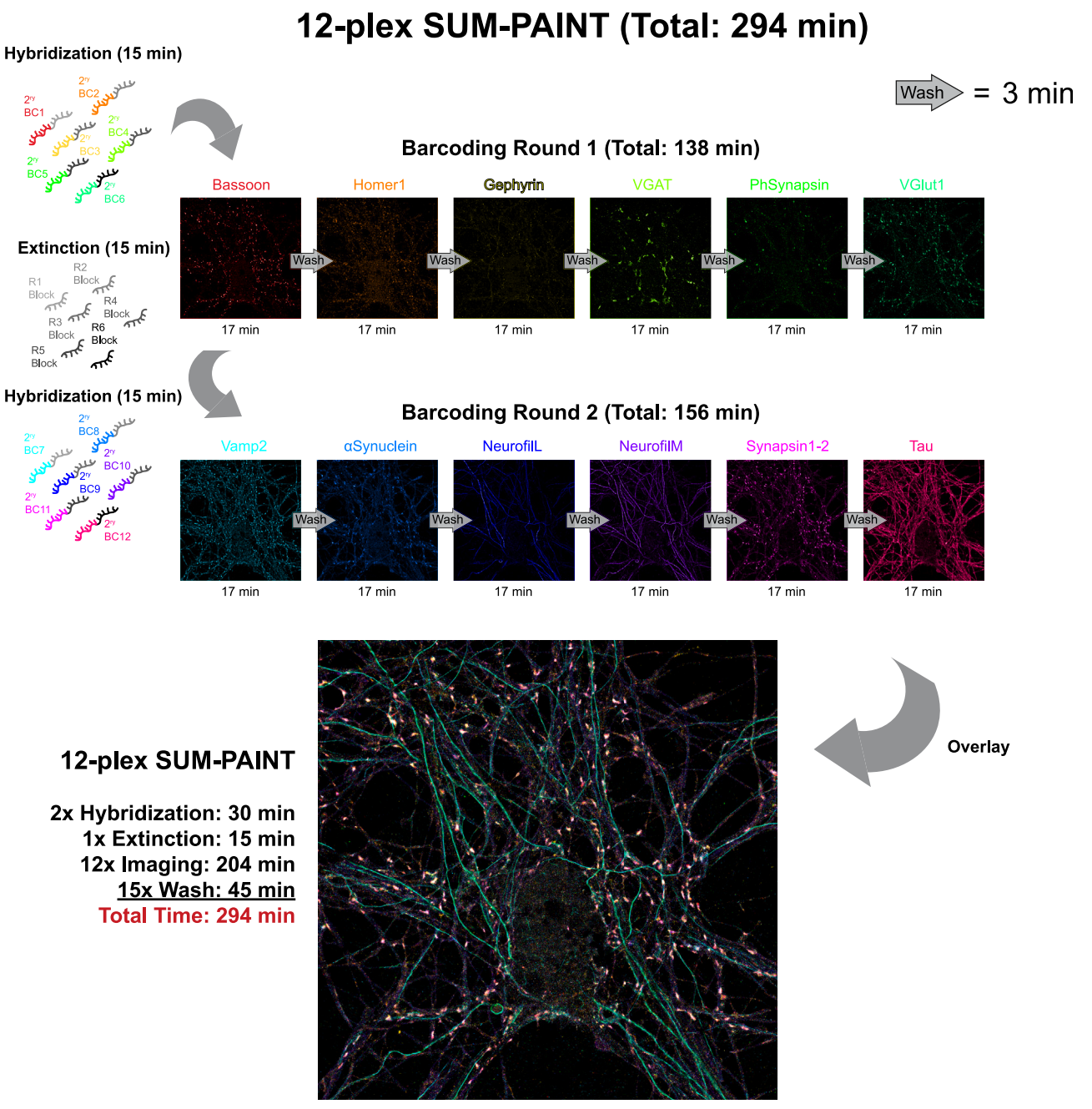

Figure S2. 12-plex SUM-PAINT demonstration, related to Figure 3

Exemplary 12-plex SUM-PAINT imaging workflow and result. 12-plex SUM-PAINT imaging can be completed in roughly 5 h. Hybridization time is 15 min followed by 6 × 17 min of super-resolved imaging with R1 to R6 sequences in barcoding round 1. Subsequent signal extinction is done by blocking strand hybridization (15 min) and followed by the hybridization of the second-round labels. Barcoding round 2 is then carried out in the same way as round one (6 × 17 min) resulting in a total experiment time of 294 min. Images show the individual protein targets and their composite 12-plex overlay.

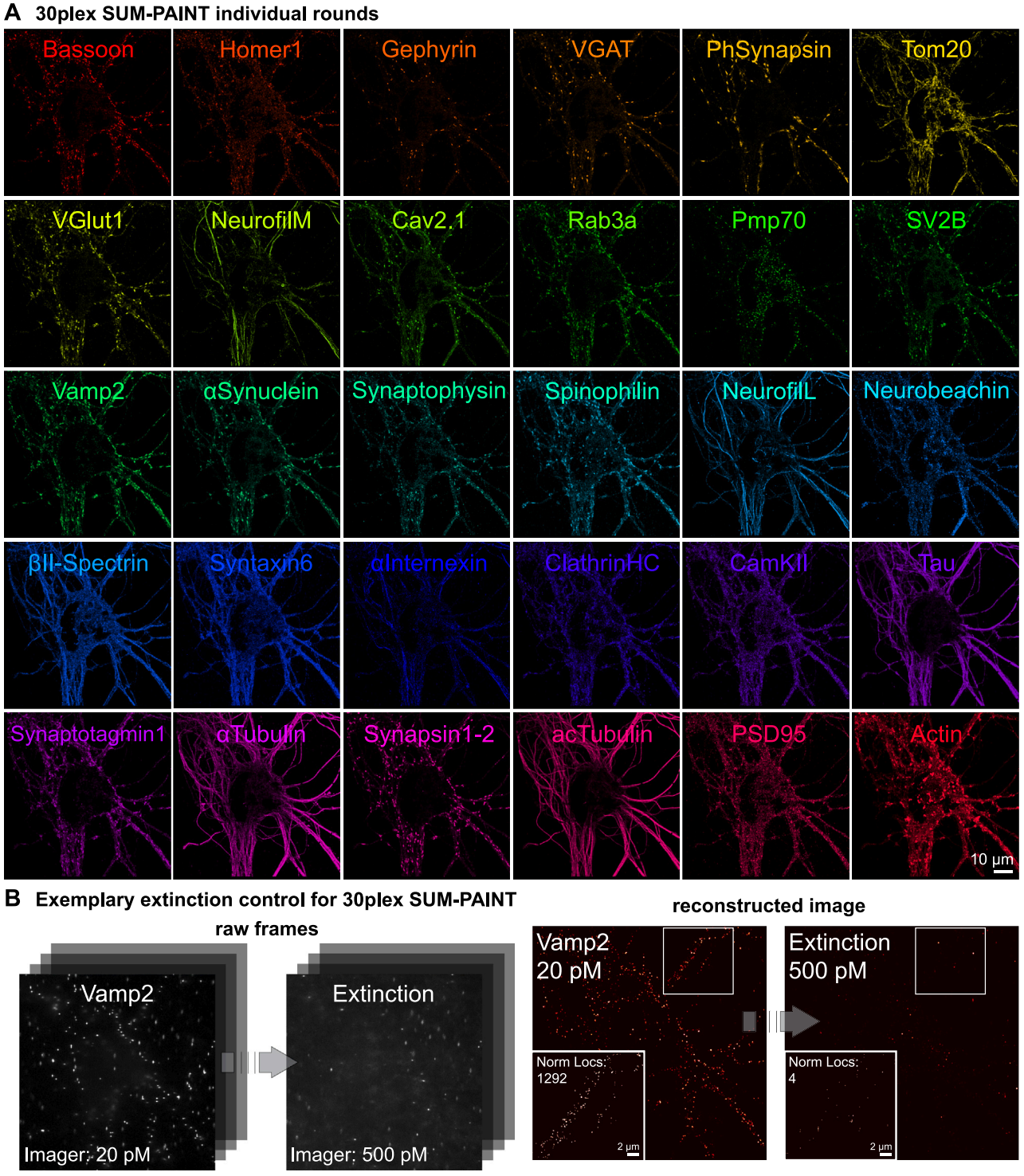

Figure S3. Gallery of individual protein targets of the 30-plex SUM-PAINT experiment and extinction controls, related to Figure 3

(A) DNA-PAINT imaging rounds were completed in 17 min for each protein target yielding an average localization precision of 6.6 nm. The protein targets range from synaptic scaffold proteins (Bassoon, Homer1, Gephyrin, PSD95) to vesicle pool proteins (e.g., VGlut1, VGAT, Vamp2, Synaptotagmin1) to organelle markers (Tom20, Pmp70) and to cytoskeleton proteins (e.g., βII-Spectrin, ac-Tubulin, NeurofilamentM/L, Actin).

(B) Exemplary extinction control round performed after each set of 6 targets in the 30plex experiment. The controls were taken with 500 p.m. imager concentration for the target exhibiting the strongest signal. Respective raw frames and the reconstructed image indicate indicate near to full extinction of the signal (over 99% extinction with localization number normalized to the imager concentration).

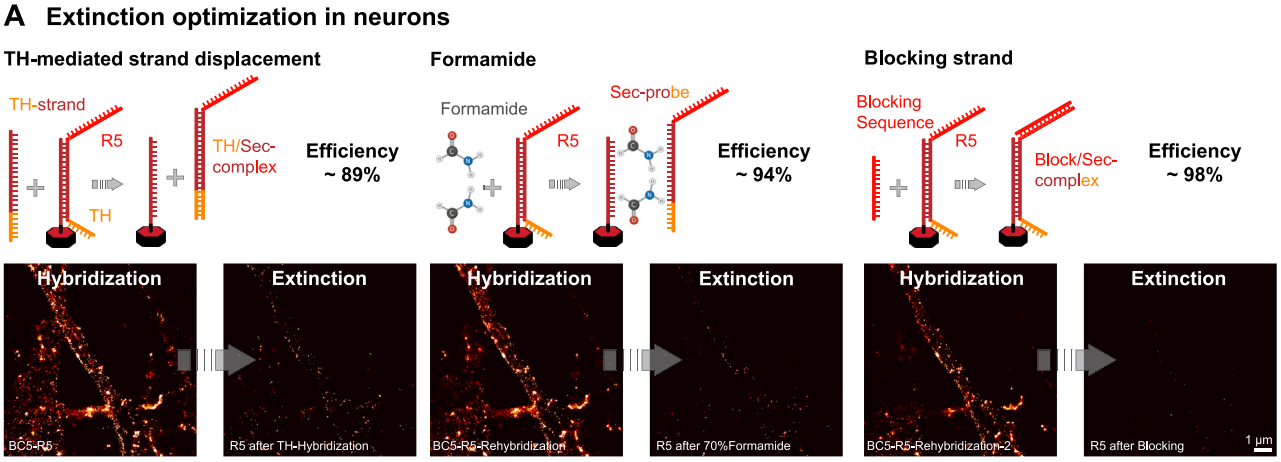

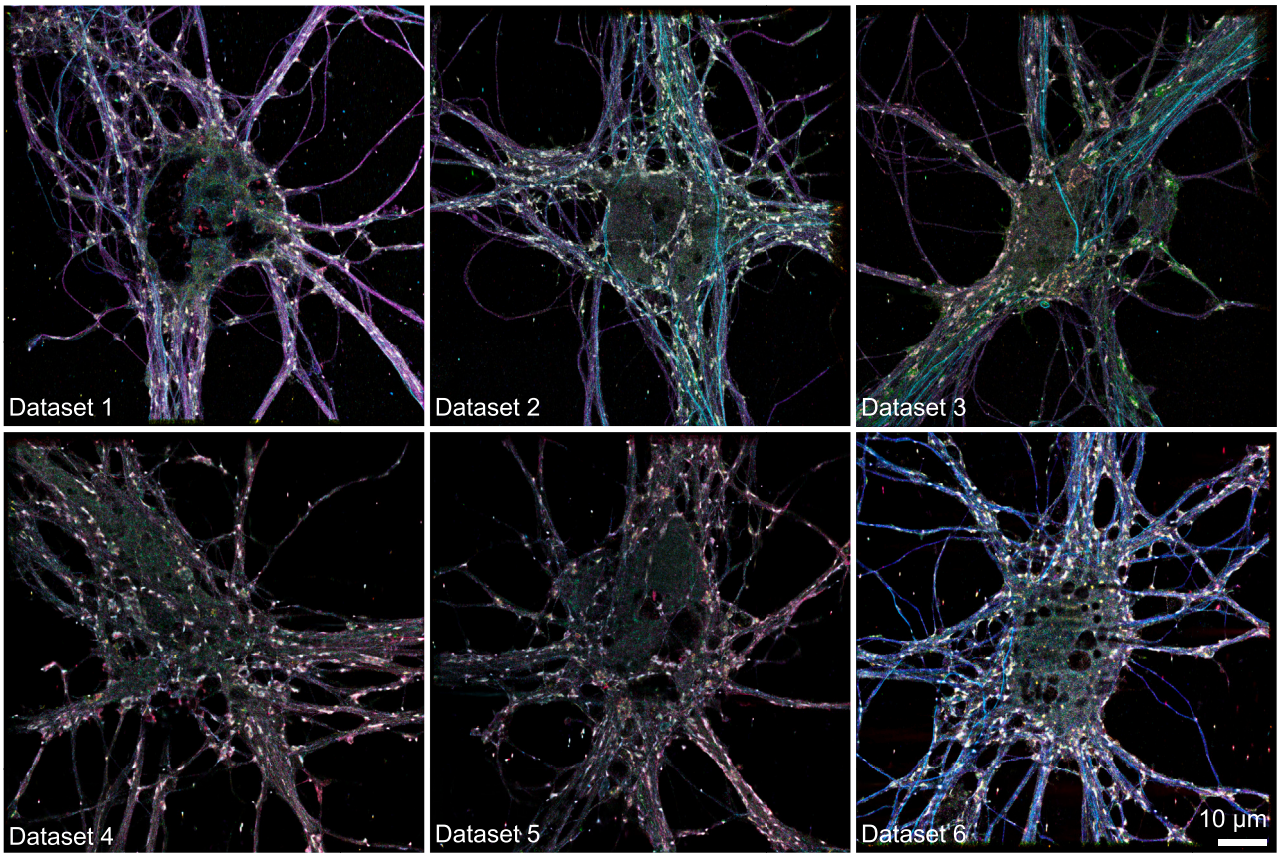

Figure S4. Signal extinction optimization in neurons and six multiplexed neuron atlas datasets, related to Figures 3 and 5

(A) Signal extinction optimization in neurons. Extinction in neurons is evaluated using three different methods, signal removal by toehold(TH)-mediated strand displacement, signal removal by formamide denaturing agent and signal blocking by blocking strand hybridization. The extinction efficiency is calculated as the remaining signal in the exemplary field of view compared to the hybridized or re-hybridized signal.

(B) Six multiplexed neuron datasets. Each dataset was imaged with at least 19 different protein targets (see Table S3).

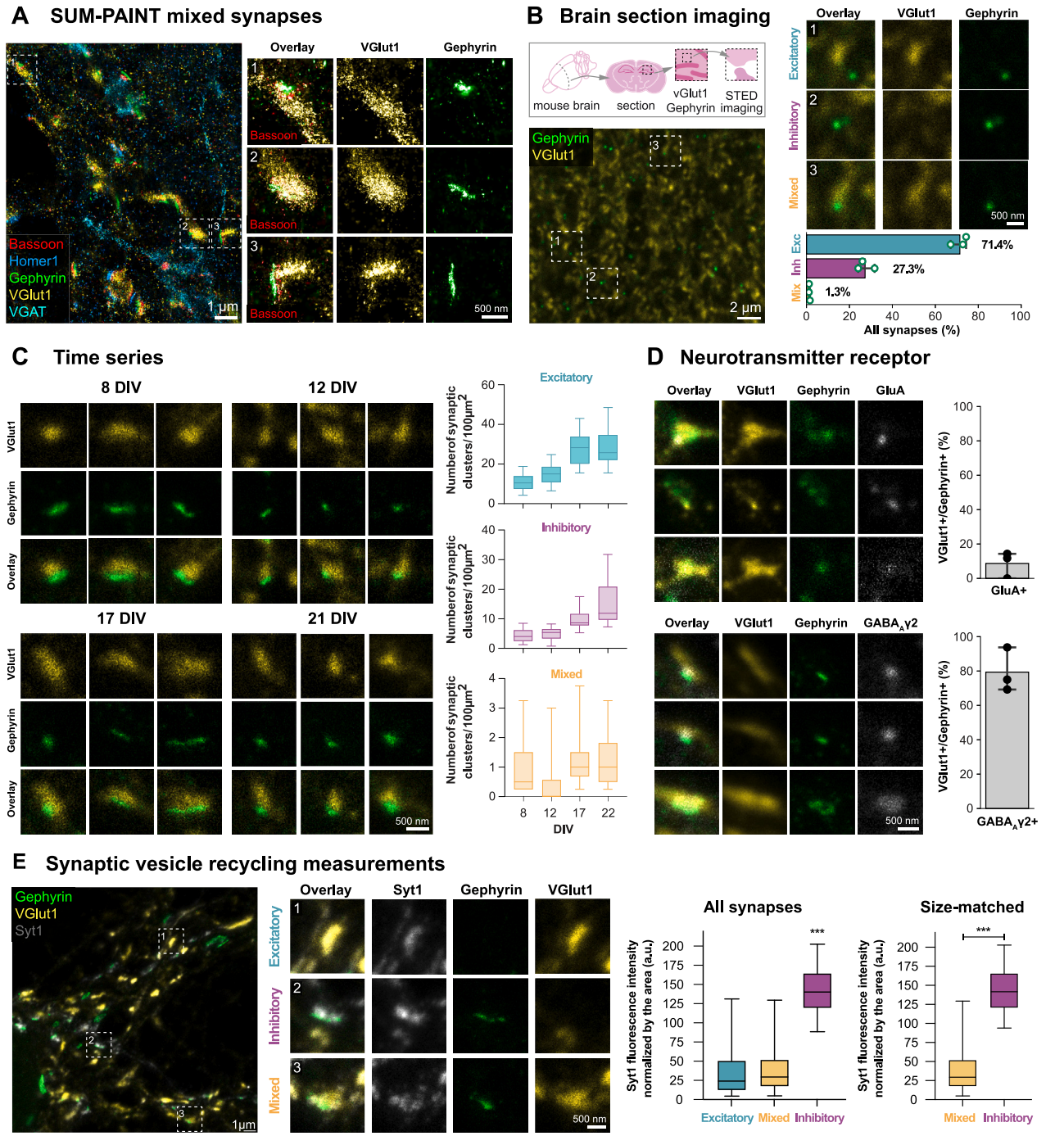

Figure S5. Characterization of the mixed synapse, related to Figure 5

(A) 5-plex super-resolved overlay of synaptic scaffold proteins Bassoon, Homer1 and Gephyrin with NTT markers VGlut1 and VGAT next to three exemplary mixed synapses. Mixed synapses are shown with separated Gephyrin (green) and VGlut1 (yellow) channels and an overlay with Bassoon (red) in addition.

(B) Brain section imaging with 2-color STED microscopy. The upper left scheme indicates the location of the imaged region in the mouse hippocampus (*stratum radiatum*). The bottom left panel shows a 2-color overlay of an exemplary hippocampal region with Gephyrin (green) and VGlut1 (yellow). The right panels show three exemplary mixed synapses with Gephyrin and VGlut1 both as single channels and in a merged overlay. The quantification shows the abundance of the three types of synapses in the brain sections.

(C) Time series evaluating the possible developmental effect on the abundance of the mixed synapse type revealed with STED microscopy. DIV 7, 12, 15 and 21 neurons were imaged with 2-color STED microscopy with three representative mixed synapses for each time-step. The overall evaluation of synaptic puncta is shown in three box-plots for excitatory, inhibitory and mixed puncta, indicating that overall synaptic puncta numbers rise until DIV 17, while the mixed class stays at a constant low abundance of about one synapse per 100 μm^2.

(legend continued on next page)

(D) Postsynaptic neurotransmitter receptor characterization for the mixed synapse type. 3-color STED imaging with VGlut1 (yellow), Gephyrin (green) and the postsynaptic receptors GluA1 (gray) or $GABA_A\gamma2$ (gray) with three exemplary mixed synapses for each experiment. The evaluation shows that ~9% of the mixed synapses express GluA as a postsynaptic receptor, while ~79% express $GABA_A\gamma2$.

(E) Synaptic vesicles in the mixed-type synapses are actively recycling and show similar recycling levels to excitatory synapses. Left and middle images: exemplary region of 18 DIV hippocampal neurons live-labeled with Syt1-lum antibody, fixed and stained for VGlut1 and Gephyrin. Insets show examples of the three different types of synapses (excitatory $VGlut1^+$-$Gephyrin^-$, mixed $VGlut1^+$-$Gephyrin^+$, and inhibitory $VGlut1^-$-$Gephyrin^+$). Boxplots show quantification of the Syt1-lum antibody uptake for the different synapse types, either for all synapses (left) or for size-matched synapses (right). In both cases the mixed type shows lower recycling properties than the inhibitory type, resembling excitatory pre-synapses. Data shown as boxplots with whiskers representing 5^{th} and 95^{th} percentile. One-way ANOVA, Tukey's *post-hoc* test vs. the other two conditions (left) or Student's *t* test (right), $p < 0.001$ (***).

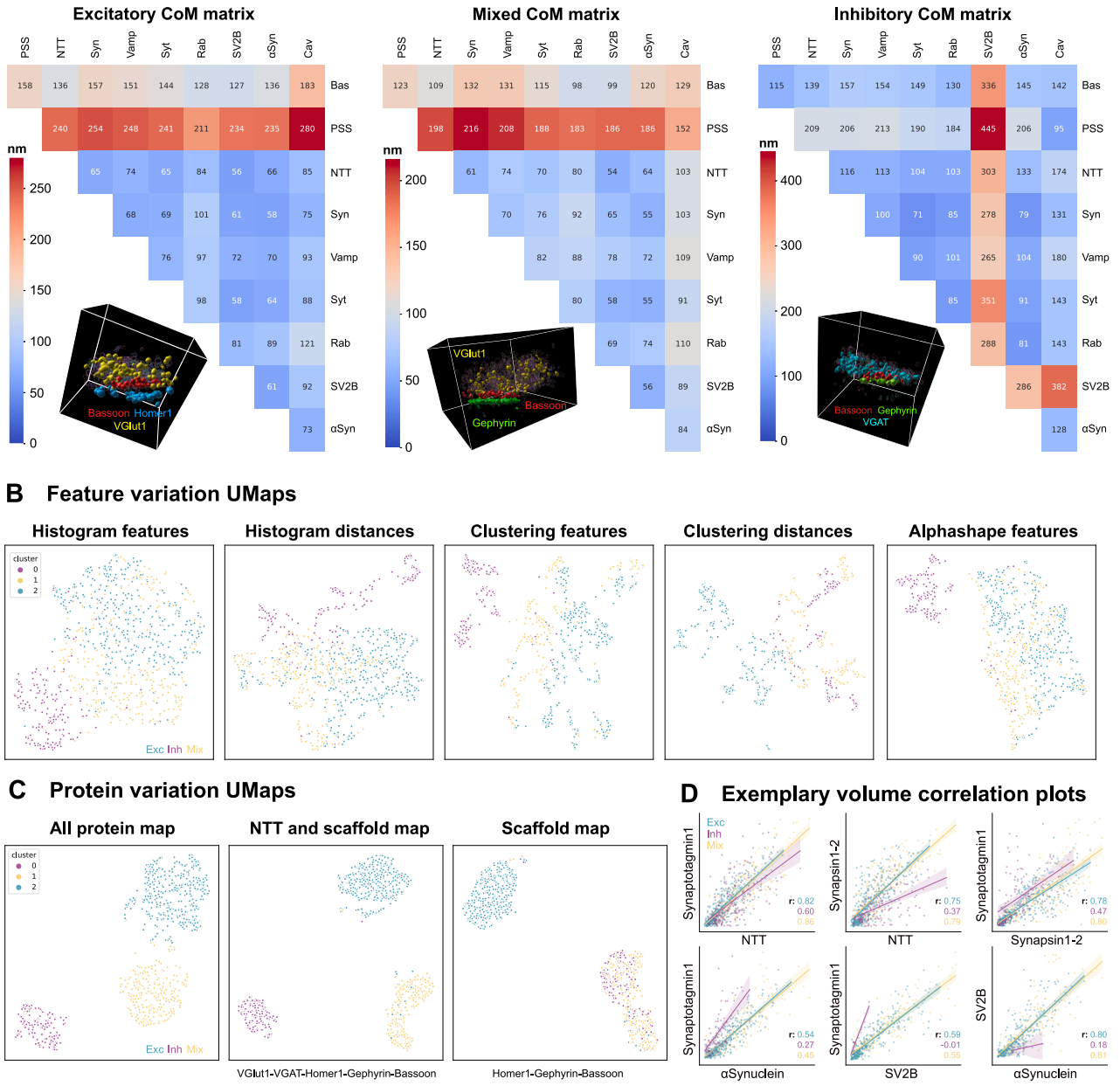

Figure S6. Multi-feature exploration of SUM-PAINT datasets, related to Figure 6

(A) Average Center-of-Mass (CoM) distance matrices for excitatory, inhibitory and mixed synapses, respectively. The distances for the protein clusters CoM were calculated for each synapse individually and the average of all excitatory (411), inhibitory (189) and mixed (297) synapses were subsequently assembled into a 9x9 matrix.

(B) UMaps for the features separated in the major classes of histogram features, histogram distances, clustering features, clustering distances and alphashape features.

(C) UMaps for selected proteins separated into all proteins, scaffold proteins and neurotransmitter transporter proteins (Bassoon, Homer1, Gephyrin, VGlut1 and VGAT) and only scaffold proteins (Bassoon, Homer1 and Gephyrin).

(D) Exemplary Pearson's correlation plots for the volume correlation. The ratio of the volume of two proteins is plotted for all synapses. Only points in which the volume was detected by cluster analysis are plotted, while the ones showing no cluster were not plotted but also are considered when performing the fit. An R value close to one indicates a strong correlation for the two considered proteins.